

Lithium isotopes within the *ab initio* no-core full configuration approach

Chase Cockrell,* James P. Vary,† and Pieter Maris‡

Department of Physics and Astronomy, Iowa State University, Ames, IA 50011

(Dated: November 10, 2018)

We perform no-core full configuration calculations for the Lithium isotopes, ${}^6\text{Li}$, ${}^7\text{Li}$, and ${}^8\text{Li}$ with the realistic nucleon-nucleon interaction JISP16. We obtain a set of observables, such as spectra, radii, multipole moments, transition probabilities, etc., and compare with experiment where available. We also present one-body density distributions for selected states. Convergence properties of these density distributions shed light on the convergence properties of one-body observables. We obtain underbinding by 0.5 MeV, 0.7 MeV, and 1.0 MeV for ${}^6\text{Li}$, ${}^7\text{Li}$, ${}^8\text{Li}$ respectively. Magnetic moments are well-converged and agree with experiment to within 20%.

PACS numbers: 21.60.De, 21.10.-k, 27.20.+n, 21.10.Ky, 21.10.Ft

I. INTRODUCTION AND MOTIVATION

The rapid development of *ab initio* methods for solving finite nuclei has opened a range of nuclear phenomena that can be evaluated to high precision using realistic inter-nucleon interactions. Here we investigate three Li isotopes through direct solution of the nuclear many-body problem with the JISP16 nucleon-nucleon (NN) interaction [1–3] by diagonalization in a sufficiently large basis space that converged binding energies are accessed by simple extrapolation. The many-body approach we adopt is referred to as the no-core full configuration (NCFC) method [4–6] which yields uncertainty estimates for binding energies.

We adopt the traditional harmonic oscillator (HO) basis which enables us to isolate and remove spurious effects of center of mass (cm) motion from all observables and from the one-body density matrices (OBDMs) to high precision. Since we address light nuclei, we feel this capability is an important ingredient. A further advantage in using the (HO) basis is its ease in performing analytical evaluations and straightforward matrix element calculations though certain alternative basis choices also have these advantages [7, 8]. In this context, the NCFC approach is similar to the no-core shell model (NCSM) [9]. The main differences are that in the NCFC approach we do not use the Lee–Suzuki renormalization procedure [10] which is commonly employed in the NCSM; and more importantly, we estimate the numerical accuracy of our results based on the rate of convergence and dependence on the basis space parameters [5, 6].

We use a set of finite single-particle HO bases, characterized by two basis space parameters, the HO energy $\hbar\Omega$ and the many-body basis space cutoff N_{max} . N_{max} is defined as the maximum number of total oscillator quanta allowed in the many-body basis space above the minimum for that nucleus. Independence of both param-

eters $\hbar\Omega$ and N_{max} signals numerical convergence; for bound states, true convergence is generally expected to be reached in the limit of a complete (infinite dimensional) basis. For the binding energy we use an extrapolation to the complete basis space, with error bars reflecting the uncertainty due to the extrapolation.

In this work, we look at the actual nucleon densities, in addition to observables such as spectra, radii, and multipole moments. In order to do so, we introduce a technique for unfolding the cm motion from the one-body density. This allows us to obtain the translationally-invariant densities, without any smearing effects from the cm motion. Indeed, salient details of the density are often enhanced in the translationally-invariant (ti) density, compared to the single-particle densities that are commonly used in configuration interaction calculations, as we will show.

II. METHODS AND INGREDIENTS

A. Nuclear Hamiltonian

We begin with the translationally-invariant Hamiltonian for the A -body system in relative coordinates

$$H_A = T_{\text{rel}} + V = \frac{1}{A} \sum_{i < j} \frac{(\vec{p}_i - \vec{p}_j)^2}{2m} + \sum_{i < j} V_{NN}(\vec{r}_i - \vec{r}_j) + \sum_{i < j} V_C(\vec{r}_i - \vec{r}_j), \quad (1)$$

where mc^2 is the nucleon mass times the speed of light (c) squared (taken to be 938.92 MeV, the average of the proton and neutron masses), V_{NN} is the NN interaction, and V_C is the Coulomb interaction, which acts between the protons only. We adopted the NN interaction JISP16, a realistic NN interaction initially developed from NN data using inverse scattering techniques. It is then adjusted with phase-shift equivalent unitary transformations to describe light nuclei without explicit three-body interactions [1–3].

JISP16 provides good convergence rates for the ground state (gs) energies of nuclei with $A \leq 16$. We investigate

*cockrell@iastate.edu

†jpvary@iastate.edu

‡pmaris@iastate.edu

convergence rates for a selection of additional observables in the present work, in particular the spectra, radii, and multipole moments. We use the naive point-like operators for these observables; we do not take effects such as meson-exchange currents into account. However, it is known that these effects can cause significant corrections to observables such as magnetic moments [11]. We should therefore expect similar deviations from experiments for our calculations of these observables.

B. No-Core Full Configuration calculations

In the many-body framework that we are using, we expand the nuclear wavefunction Ψ in a basis of Slater determinants of single-particle HO states. Note that we use single-particle coordinates, rather than relative coordinates, in the nuclear wavefunction. That means that our wavefunctions, and therefore our OBDMs calculated as expectation values of one-body operators, will include cm motion.

All many-body basis states are included with HO quanta up to and including the amount governed by the N_{\max} truncation. Thus, if the highest HO single-particle state for the minimal HO configuration has N_0 HO quanta, then the highest allowed single-particle state in the truncated basis will have $N_0 + N_{\max}$ HO quanta. Furthermore, our calculations are 'No-Core' configuration interaction calculations. This means that all nucleons participate in the interactions on an equal footing. As we increase N_{\max} , and approach convergence, we expect physical observables to become independent of both the HO parameter $\hbar\Omega$ and the truncation parameter N_{\max} . However, due to current limits to our finite basis, our calculations do show some parameter dependence, even in the largest basis spaces. We apply previously established extrapolation tools to take the continuum limit of the binding energy as we discuss shortly.

The HO basis for single-particle states, in combination with this many-particle N_{\max} truncation, leads to exact factorization of the nuclear wavefunctions into a cm wavefunction and a ti wavefunction

$$\Psi(\vec{r}_i) = \Phi_{\text{cm}}^{\Omega}(\vec{R}) \otimes \phi_{\text{ti}} \quad (2)$$

where $\vec{R} = (\frac{1}{A}) \sum_{i=1}^A \vec{r}_i$ and ϕ_{ti} depends only on inter-nucleon coordinates. The actual Hamiltonian that we are using involves adding and subtracting H_{cm} so that H_A takes the form

$$\begin{aligned} H_A &= \sum_{i<j}^A \left[\frac{(\vec{p}_i - \vec{p}_j)^2}{2mA} + V_{ij} \right] \\ &= \sum_{i=1}^A \left[\frac{p_i^2}{2m} + \frac{1}{2} m\Omega^2 r_i^2 \right] \\ &\quad + \sum_{i<j}^A \left[V_{ij} - \frac{m\Omega^2}{2A} (\vec{r}_i - \vec{r}_j)^2 \right] - H_{\text{cm}} \quad (3) \end{aligned}$$

In order to separate the cm excited states from the low-lying states of interest, we adopt the Lawson method [12] whereby we add a Lagrange multiplier term, $\lambda(H_{\text{cm}}^{\Omega} - \frac{3}{2}\hbar\Omega)$, to the many-body Hamiltonian, Eq. (3)

$$H = H_A + \lambda(H_{\text{cm}} - \frac{3}{2}\hbar\Omega). \quad (4)$$

With λ positive, states with cm excitations are separated by multiples of $\lambda\hbar\Omega$ from the states with the lowest HO cm motion. Since the Lagrange multiplier term acts only on the cm coordinate, it is independent of the inter-nucleon coordinates and it does not affect the energy eigenvalues or the translationally-invariant wavefunctions ϕ_{ti} of the low-lying states. Indeed, observables for the low-lying states are independent of λ , as long as $\lambda\hbar\Omega$ is much larger than the excitation energy of the highest state of interest.

In the truncated basis space, we can now write the many-body Schrödinger equation as a finite matrix equation with a real, symmetric, sparse matrix. The eigenvalues of this matrix give us the binding energy, and the corresponding eigenvectors give us the wavefunctions. In any finite basis space, the eigen-energies satisfy the variational principle and show uniform and monotonic convergence from above with increasing N_{\max} , allowing for extrapolation to the infinite basis space. To obtain the extrapolated gs energy $E_{gs}(\infty)$, we use a fitting function of the form

$$E_{gs}(N_{\max}) = a \exp(-c N_{\max}) + E_{gs}(\infty). \quad (5)$$

This is an empirical method [4-6] that is valid within estimated uncertainties that we now define. We assign equal weight to each of three successive values of N_{\max} at a fixed $\hbar\Omega$ and perform a regression analysis. The difference between extrapolated results from two consecutive sets of three N_{\max} values is used as the estimate of numerical uncertainty associated with the extrapolation. The optimal $\hbar\Omega$ value for this extrapolation appears to be the $\hbar\Omega$ that minimizes the difference between the extrapolated energy and the result at the largest N_{\max} . Typically, this corresponds to a $\hbar\Omega$ value slightly above the variational minimum. Of course, the extrapolated results should be independent of $\hbar\Omega$, within their numerical error estimates, and we do check for such consistency. Furthermore, we often adjust our numerical error estimate by considering the results over a range of 5 MeV in $\hbar\Omega$.

For other observables, we do not have a robust and reliable extrapolation method; we therefore use the degree of (in)dependence from the basis space parameters $\hbar\Omega$ and N_{\max} as a measure for convergence as we describe further below on a case-by-case basis.

For nuclei with mass $A > 4$, it is challenging to obtain convergence (independence of both N_{\max} and Ω) for all observables within the NCFC approach with realistic interactions. As N_{\max} increases, the dimension of the many-body basis increases exponentially, and there is a

clear need for high-performance computing. For the Li isotopes we investigate here, we have limited the basis space to about 1 billion: for ${}^6\text{Li}$ the largest basis space is $N_{\text{max}} = 16$, with a dimension of 805,583,856; for ${}^7\text{Li}$ the largest basis space is $N_{\text{max}} = 14$, with a dimension of 1,244,131,981; and for ${}^8\text{Li}$ the largest basis space is $N_{\text{max}} = 12$, with a dimension of 1,222,330,036. We use the code MFDn (Many Fermion Dynamics for nuclear structure) [13, 14], which is a state-of-the-art numerical code for no-core configuration interaction calculations. The calculations were performed on the Cray XT4 and XE6 at the National Energy Research Supercomputer Center (NERSC), using up to 8,000 processors (4 or 6 cores/processor) with 8 GB of memory each.

C. One-Body Density Matrix

The OBDM represents, in a compact form, sufficient information about quantum states of a system to evaluate all observables that can be expressed by one-body operators. For example, a single wavefunction of ${}^6\text{Li}$ at $N_{\text{max}} = 16$ has a size of 5 GB, while the OBDM for a single state in that same basis is less than 5 MB. The OBDMs also provide the necessary information for visualizing nuclear density distributions as we demonstrate below.

The non-local one-body density in coordinate space for an initial A -body wavefunction Ψ_i and final A -body wavefunction Ψ_f is defined as

$$\rho^{fi}(\vec{r}_1, \vec{r}'_1) = \int \Psi_f^*(\vec{r}_1, \vec{r}_2, \dots, \vec{r}_A) \times \Psi_i(\vec{r}'_1, \vec{r}_2, \dots, \vec{r}_A) d^3r_2 \dots d^3r_A. \quad (6)$$

The limit $\vec{r}'_1 = \vec{r}_1$ of Eq. (6) gives the local one-body density. For $\Psi_f = \Psi_i$ this corresponds to the probability of finding a nucleon at position \vec{r}_1 when the system is in that state. That is, the local one-body density distribution is given by

$$\rho_{\text{sf}}^\Omega(\vec{r}_1) = \int \rho(\vec{r}_1, \vec{r}'_1) \delta(\vec{r}_1 - \vec{r}'_1) d^3r'_1 \quad (7)$$

where we suppress the state labels for simplicity and insert a superscript Ω to signify the dependence on the HO basis space used in the evaluation of the eigenfunctions. Since it depends on the single-particle coordinates, we refer to this density as the space-fixed (sf) density.

Note that, due to our use of single-particle coordinates, rather than relative coordinates, our wavefunctions $\Psi(\vec{r}_i)$ include cm motion. The resulting one-body density distributions will therefore include contributions from the cm motion. However, because of the exact factorization of the cm wavefunction and the ti wavefunction (see Eq. (2)) this density is actually a convolution of the cm density ρ_{cm}^Ω and the ti density $\rho_{\text{ti}}(\vec{r})$ describing the probability of finding a nucleon at position \vec{r} relative to the

cm of the entire nucleus¹

$$\rho_{\text{sf}}^\Omega(\vec{r}_1) = \int \rho_{\text{ti}}(\vec{r}_1 - \vec{R}) \rho_{\text{cm}}^\Omega(\vec{R}) d^3\vec{R}. \quad (8)$$

For the HO basis, ρ_{cm}^Ω is a simple Gaussian (the gs density of H_{cm}) with explicit dependence on Ω that smears out ρ_{ti} . This smearing can obfuscate interesting details of ρ_{ti} . Furthermore, it introduces a spurious dependence on the basis parameter Ω into ρ_{sf}^Ω that masks the convergence. Even in the limit of a completely converged calculation, the single-particle density ρ_{sf}^Ω depends on Ω , whereas ρ_{ti} becomes independent of the basis.

In order to eliminate these smearing effects and to help develop a physical intuition for the *ab initio* structure of a nucleus, it would be helpful to see the coordinate space density distributions free of spurious cm motion. This can be achieved by a deconvolution of the cm density and the ti density using standard Fourier methods [15]

$$\rho_{\text{ti}}(\vec{r}_1) = F^{-1} \left[\frac{F[\rho_{\text{sf}}^\Omega(\vec{r}_1)]}{F[\rho_{\text{cm}}^\Omega(\vec{R})]} \right] \quad (9)$$

where $F[f(\vec{r})]$ is the 3-dimensional Fourier transform of $f(\vec{r})$. At convergence, the dependence on Ω should cancel on the RHS of this equation. That means that after this deconvolution, we can better investigate the convergence of the physically-relevant ti density.

In addition to the 3-dimensional ti densities, we also show results for different multipoles of the ti density, $\rho_{\text{ti}}^{(K)}(r)$, defined with the same initial and final states, having total angular momentum J and magnetic projection M , as

$$\rho_{\text{ti}}(\vec{r}) = \sum_{K=0}^{2J} \frac{\langle JMK0|JM \rangle}{\sqrt{2J+1}} Y_K^{*0}(\hat{r}) \rho_{\text{ti}}^{(K)}(r). \quad (10)$$

These multipoles allow for a better assessment of the numerical convergence of the densities, as we will illustrate below. Another advantage of the multipole expansion is that it allows for a straightforward determination of the ti density for any M : the multipoles $\rho_{\text{ti}}^{(K)}(r)$ are independent of M . However, some features of the density, in particular clustering, are more apparent from the 3-dimensional plots of $\rho(\vec{r})$ than from plots of the different multipole components.

The results we present here for densities of the Li isotopes are all translationally-invariant unless we state otherwise. An alternative method to isolate the ti density has been developed in [17].

¹ Note that our ti density is not the same as the one-body density in Jacobi coordinates, $\sigma(\vec{\xi})$ as defined in Ref. [16], which describes the probability of finding one nucleon at $\vec{\xi}$ relative to the cm of the remaining $A-1$ nucleons. Both these densities are translationally-invariant, and they are related to each other via rescaling factors $\frac{A}{A-1}$.

D. Observables

In HO space, the space-fixed OBDM is specified by its matrix elements

$$\rho_{\beta\alpha}^{fi} = \langle \Psi_f | a_\alpha^\dagger a_\beta | \Psi_i \rangle, \quad (11)$$

where α and β stand for a set of single-particle quantum numbers $(n_\alpha, l_\alpha, j_\alpha, m_\alpha, \tau_{z,\alpha})$ and $(n_\beta, l_\beta, j_\beta, m_\beta, \tau_{z,\beta})$, and we use the Dirac bra-ket notation to represent the total many-body state vector. Once we have obtained the one-body density matrix elements $\rho_{\beta\alpha}$ (OBDMs), we can easily calculate observables that can be expressed as one-body operators. For initial and final states with total angular momentum $J_{i,f}$ and possibly additional quantum numbers $\lambda_{i,f}$, but with the same magnetic projection M , the E2 matrix elements using the canonical one-body electromagnetic current operator are given by

$$\begin{aligned} M_{E2}^{fi} &= \langle \lambda_f J_f M | E2 | \lambda_i J_i M \rangle \\ &= \sum_{\alpha\beta} \rho_{\beta\alpha}^{fi} \langle \alpha | \int r^2 Y_2^0(\hat{r}) d^3r | \beta \rangle, \end{aligned} \quad (12)$$

with α and β restricted to the protons only ($\tau_z = \frac{1}{2}$). Note that the fact that the OBDM includes cm motion does not matter for E2 matrix elements (nor for M1 matrix elements discussed below): the cm wavefunction is a normalized s-wave, and does not contribute to the integral due to the factor $Y_2^0(\hat{r})$.

For comparison with experiments, it is more convenient to convert these M -dependent matrix elements to reduced matrix elements using the Wigner–Eckart theorem [18]. For a proper tensor operator T_{Kk} the reduced matrix element is defined by

$$\begin{aligned} \langle \lambda_f J_f || T_K || \lambda_i J_i \rangle &= \langle \lambda_f J_f M_f | T_{Kk} | \lambda_i J_i M_i \rangle \\ &\times \frac{\sqrt{2J_f + 1}}{\langle J_f M_f K k | J_i M_i \rangle} \end{aligned} \quad (13)$$

provided that the Clebsch–Gordan coefficient in the denominator, $\langle J_f M_f K k | J_i M_i \rangle$ (following the conventions of Ref. [18]), is not zero. In terms of the reduced E2 matrix elements, reduced E2 transition probabilities are given by [19]

$$B(E2; i \rightarrow f) = \frac{1}{2J_i + 1} \langle \lambda_f J_f || E2 || \lambda_i J_i \rangle^2 \quad (14)$$

in units $e^2 \text{fm}^4$. The quadrupole moment is conventionally defined through the E2 matrix element for $M = J$

$$Q = \left(\frac{16\pi}{5} \right)^{1/2} \langle \lambda J M = J | E2 | \lambda J M = J \rangle \quad (15)$$

and can also be expressed in terms of the reduced matrix element as [19]

$$Q = \left(\frac{16\pi}{5} \right)^{1/2} \frac{\langle J J 2 0 | J J \rangle}{\sqrt{2J + 1}} \langle \lambda J || E2 || \lambda J \rangle \quad (16)$$

in units $e \text{fm}^2$.

The matrix elements for the M1 transitions and magnetic moments receive contributions both from the proton and neutron intrinsic spins and from the proton orbital motion. Again, we consider only the canonical one-body electromagnetic current operator, in which case they can be calculated from the OBDMs

$$\begin{aligned} M_{M1}^{fi} &= \langle \lambda_f J_f M | M1 | \lambda_i J_i M \rangle \\ &= \sum_{\alpha\beta} \rho_{\beta\alpha}^{fi} \langle \alpha | \frac{1}{2}(1 + \tau_z)(L + g_p \sigma) + \frac{1}{2}(1 - \tau_z)g_n \sigma | \beta \rangle \end{aligned}$$

where $g_p = 5.586$ and $g_n = -3.826$ are the proton and neutron gyromagnetic ratios in nuclear magneton (μ_N) units; the quantities L , σ and τ represent the conventional orbital angular momentum, spin and isospin operators. In terms of the reduced M1 matrix element, the reduced M1 transition probabilities are given as [19]

$$B(M1; i \rightarrow f) = \frac{1}{2J_i + 1} \langle \lambda_f J_f || M1 || \lambda_i J_i \rangle^2 \quad (17)$$

in units μ_N^2 , and the magnetic moment is defined as

$$\mu = \left(\frac{4\pi}{3} \right)^{1/2} \frac{\langle J J 1 0 | J J \rangle}{\sqrt{2J + 1}} \langle \lambda J || M1 || \lambda J \rangle \quad (18)$$

in units μ_N .

We also present results for the point-proton root-mean-square (RMS) radius, $\langle r_{pp}^2 \rangle^{1/2}$. This can be calculated either from the translationally-invariant local density, ρ_{ti} , or directly, as a two-body operator, from the wavefunction in single-particle coordinates, $\Psi(\vec{r}_i)$. We performed the calculations with both approaches and confirmed the results were identical to within the numerical precision of four significant figures.

In order to convert measured nuclear charge radii, $\langle r_c^2 \rangle^{1/2}$, to point-proton radii, we use [20]

$$\langle r_{pp}^2 \rangle = \langle r_c^2 \rangle - R_p^2 - \frac{N}{Z} R_n^2 - \frac{3\hbar^2}{4M_p^2 c^2} \quad (19)$$

Here, $R_p^2 = 0.769(12) \text{fm}^2$ is the RMS proton charge radius, $R_n^2 = -0.177(4) \text{fm}^2$ the RMS neutron charge radius, M_p the proton mass, and $\frac{3\hbar^2}{4M_p^2 c^2} \approx 0.033 \text{fm}^2$ the Darwin–Foldy correction.

In addition to these correction terms there is also a spin-orbit contribution to the charge radius, but this contribution is model-dependent, and (for the nuclei discussed here) less than 1% for realistic wavefunctions [21]. Hence we neglect it. For the experimental radii we use the values of Ref. [21], which were obtained from high-precision laser spectroscopy measurements of isotope shifts in combination with the ${}^6\text{Li}$ charge radius as absolute reference. Using the ${}^7\text{Li}$ charge radius as reference in combination with the same isotope shifts gives radii that are about 2% to 3% smaller than the ones we have listed in the tables below [22].

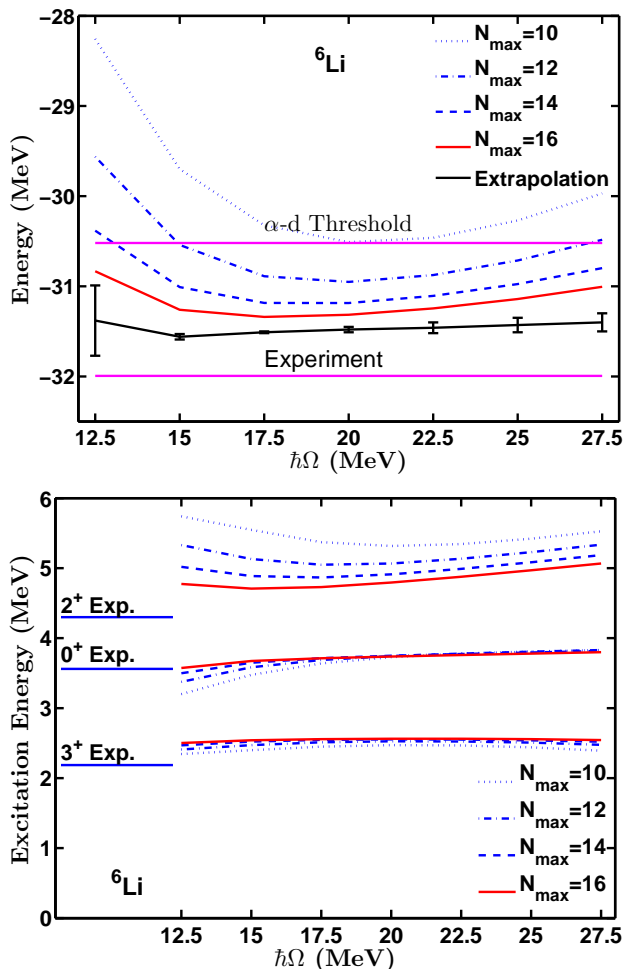


FIG. 1: (Color online) The gs energy (top) and excitation spectrum (bottom) of ${}^6\text{Li}$ for a sequence of N_{max} values (indicated in the legend) and as function of the HO energy. The extrapolated gs energy is shown at specific values of $\hbar\Omega$ with uncertainties (defined in the text) indicated as error bars.

III. RESULTS

A. ${}^6\text{Li}$

In Fig. 1, we compare the gs energy and excitation energies at a sequence of N_{max} values and as a function of the HO energy $\hbar\Omega$. We also provide the extrapolated gs energy as a function of $\hbar\Omega$ along with the assessed uncertainties (error bars) as described above.

The gs energy for ${}^6\text{Li}$ is rapidly converging as indicated by the emerging independence of the two basis parameters (N_{max} , $\hbar\Omega$). The convergence is most rapid around $\hbar\Omega = 17.5$ to 20 MeV, where the variational upper bound on the energy is minimal. Our extrapolated gs energy [5] shows that the system is underbound by 0.50 MeV. Excitation energies are well converged at higher N_{max} (12 and above) values, at least for 3^+ and 0^+ states. Note that these states are narrow resonances: the experimen-

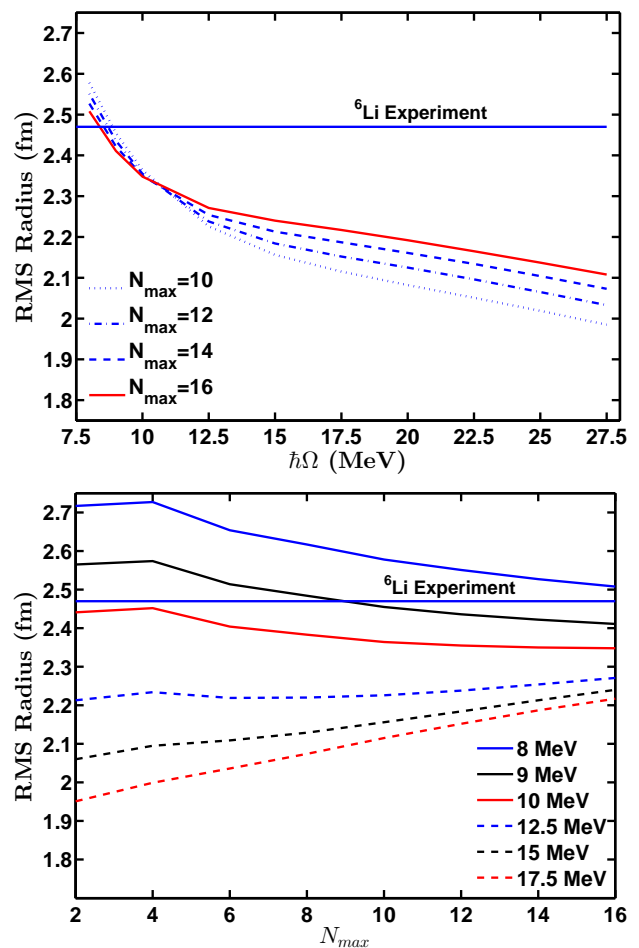


FIG. 2: (Color online) The RMS point-proton radius of the gs of ${}^6\text{Li}$ as a function of HO energy at various N_{max} values (top) and as function of N_{max} at various values of the HO energy (bottom).

tal width of the 3^+ is 24 keV and the width of the first excited 0^+ is 8 eV.

The excitation energy of the first 2^+ state is much less converged, and shows a systematic increase with increasing $\hbar\Omega$. Such $\hbar\Omega$ -dependence of the excitation energy is typical for wide resonances as observed in comparisons of NCSM results with inverse scattering analysis of α -nucleon scattering states [4, 23]. In light of these previous analyses, the significant $\hbar\Omega$ -dependence seems commensurate with the large experimental width of 1.3 MeV for this 2^+ state.

In Fig. 2, we show the dependence of the RMS point-proton radius on the basis space parameters N_{max} and $\hbar\Omega$ for ${}^6\text{Li}$. It appears that this radius is converging less rapidly than the gs and excitation energies. Furthermore, the convergence is neither monotonic nor uniform: at small values of the HO energy the radius tends to decrease with increasing N_{max} , whereas at larger values of $\hbar\Omega$ the radius increases with increasing N_{max} ; around $\hbar\Omega = 10$ to 12.5 MeV the RMS radius is nearly indepen-

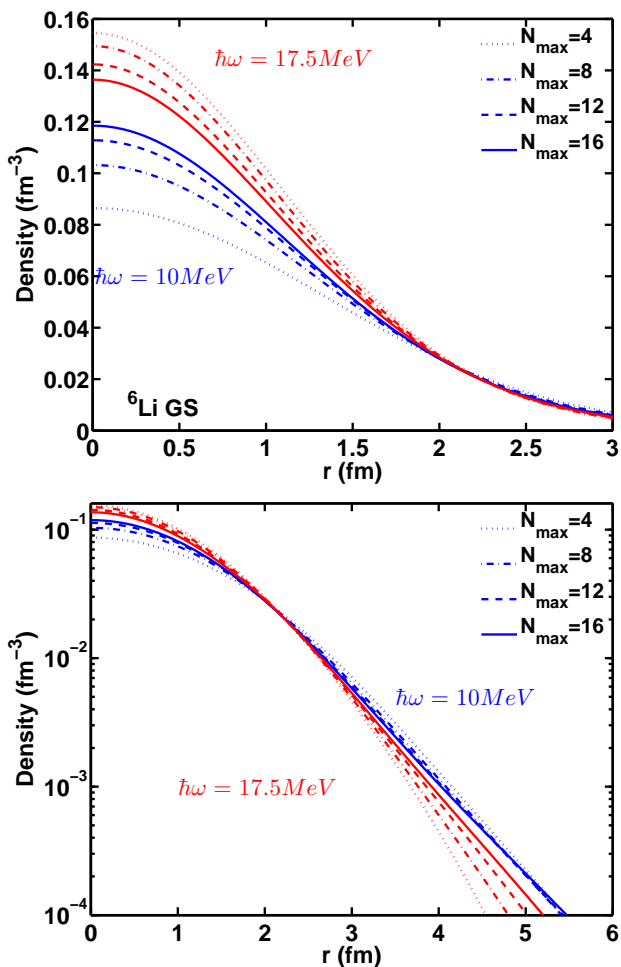


FIG. 3: (Color online) The angle-averaged density of the ${}^6\text{Li}$ gs for various N_{max} values at $\hbar\Omega = 10$ MeV (blue curves) and 17.5 MeV (red curves) on a linear (top) and semi-logarithmic (bottom) scale.

dent of N_{max} . Because of this, it is difficult to make realistic estimates of uncertainties for radii and other long-range observables such as quadrupole moments which exhibit similar patterns.

The convergence patterns shown in Fig. 2 may be understood from the following observation: since the HO wavefunctions fall off like a Gaussian, e^{-cr^2} while the true nuclear wavefunction falls off like an exponential, e^{-dr} , observables whose calculations are weighted towards the tail of the wavefunction, such as the RMS radius, will converge slower than those observables that depend less on the tails, such as the energy and the magnetic moment (see below). Furthermore, it is well known that the RMS radius, and also other long-range operators such as the quadrupole moment, are minimally affected by the short-range correlations [24, 25]. And the value of $\hbar\Omega$ that minimizes the gs energy is not necessarily the value of $\hbar\Omega$ that best represents the long-range behavior of the wavefunction.

In Fig. 3 we show the radial density distribution for two

sets of finite basis spaces, with $\hbar\Omega = 10$ and 17.5 MeV respectively. The lower panel shows that the exponential tail is much better represented in a HO basis with $\hbar\Omega = 10$ MeV than in a HO basis with 17.5 MeV, and that the long-range behavior of the one-body density is therefore converging much more rapidly in a HO basis with $\hbar\Omega = 10$ MeV, and rather poorly converging in the HO basis that minimizes the gs energy. That is, the radial density calculated with $\hbar\Omega = 10$ MeV shows much more consistent long-range behavior at the three highest N_{max} values than the density calculated with $\hbar\Omega = 17.5$ MeV. This leads us to the conclusion that while the value of $\hbar\Omega$ that minimizes the gs energy is an appropriate value when calculating gs and excitation energies, as well as magnetic observables, this value is not necessarily optimal for calculations of observables that depend primarily on long-range correlations, even in the moderately large basis spaces considered here.

Therefore we will quote results for long-range observables at the $\hbar\Omega$ value where the RMS radii for various N_{max} values intersect as seen in the top portion of Fig. 2, rather than at the $\hbar\Omega$ value that minimizes the gs energy. To be specific, for the Li-isotopes under discussion here, we simply take the results at $\hbar\Omega = 10$ to 12.5 MeV (where the N_{max} dependence appears to be minimal) as our approximation to the converged value of the RMS radius. In a similar fashion, we will cite results for the region of minimal N_{max} dependence for other observables that depend primarily on long-range correlations. Such observables include RMS radii, E2 moments, and B(E2) transitions. Robust extrapolations to the infinite basis space and reliable error estimates for these observables remain an open question.

In Fig. 4 we show the radial quadrupole component of the ${}^6\text{Li}$ gs density distribution, $\rho_{\text{ti}}^{(2)}(r)$, at $\hbar\Omega = 17.5$ MeV for several N_{max} values. From this figure it is evident that the quadrupole moment

$$\mathcal{Q} = \frac{4}{5}\sqrt{\frac{\pi}{6}} \int \rho^{(2)}(r) r^4 dr \quad (20)$$

receives both positive and negative contributions. For $N_{\text{max}} = 4$, the positive contributions are significantly larger than the small negative contribution around 2 fm, but as N_{max} increases, this negative region becomes more pronounced. At $N_{\text{max}} = 16$ the quadrupole density is nearly converged inside about 3 fm. The corresponding quadrupole moment, $\mathcal{Q} = -0.075$ e fm², appears to approach convergence. The small positive region inside 0.9 fm contributes less than 1% to this value, but about half of the contribution from the negative region between 0.9 fm and 3.4 fm is cancelled by the positive tail of the quadrupole distribution: their contributions are -0.167 e fm² and $+0.092$ e fm² respectively. Note that this positive tail is well outside the charge radius.

Table I presents a capsule view of selected spectral and other observables for ${}^6\text{Li}$. In principle, we can extrapolate not only the gs energy, but also the binding energies of the excited states to the infinite basis space. We

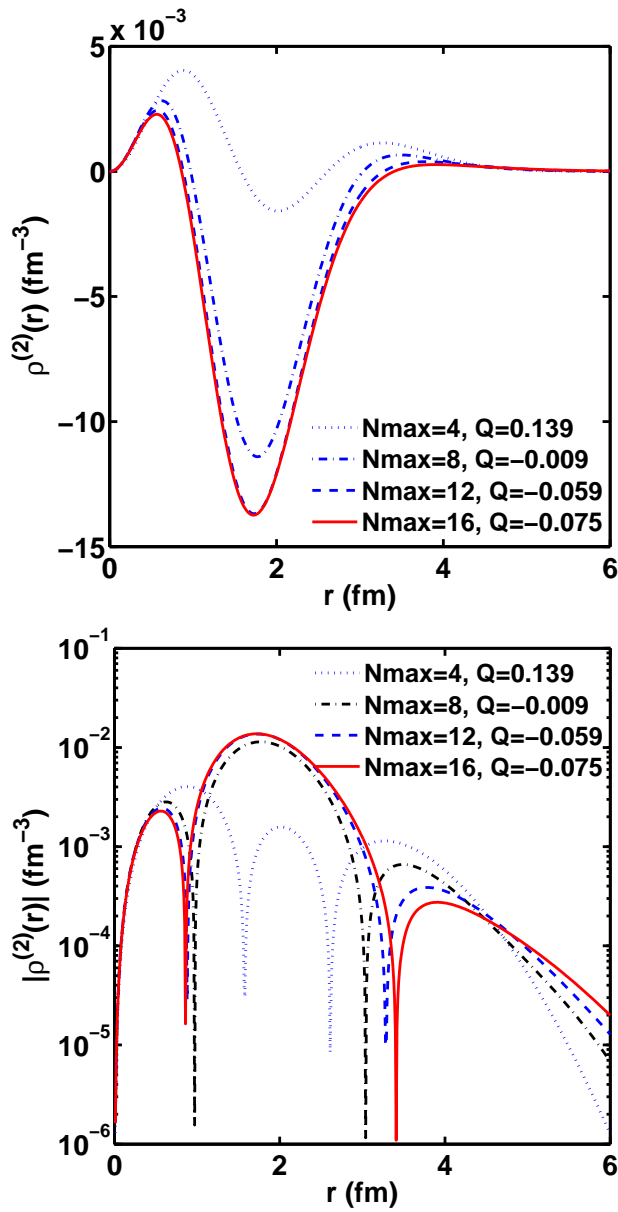


FIG. 4: (Color online) The radial quadrupole density $\rho_{\text{ti}}^{(2)}(r)$ of the ${}^6\text{Li}$ gs for various N_{max} values at $\hbar\Omega = 17.5$ MeV on a linear (top) and semi-logarithmic (bottom) scale.

can then calculate the excitation energy as the difference between the extrapolated binding energies, treating the numerical error estimates as independent. For the excitation energies that appear to be converged (in particular the 3^+ state in Fig. 1), such a procedure leads to an overestimate of the numerical uncertainty in the excitation energy: part of the numerical error is common to the ground state and the excited state. For such states we reduce the obtained numerical error estimates based on the apparent convergence of the excitation energies in finite basis spaces. On the other hand, for states with excitation energies that show a significant $\hbar\Omega$ dependence (such as the 2^+ state in Fig. 1), we increase our numerical

${}^6\text{Li}$	Expt.	JISP16	AV18/IL2	CD-B	INOY
$E_b(1^+, 0)$	31.994	31.49(3)	32.0(1)	29.07	32.3(2)
$\langle r_{pp}^2 \rangle^{1/2}$	2.45(5)	2.3	2.39(1)	2.25	2.14
$E_x(3^+, 0)$	2.186(2)	2.56(2)	2.2(2)		
$E_x(0^+, 1)$	3.56(1)	3.68(6)	3.4(2)		
$E_x(2^+, 0)$	4.312(22)	4.5(3)	4.2(2)		
$E_x(2^+, 1)$	5.366(15)	5.9(2)	5.5(2)		
$Q(1^+, 0)$	-0.082(2)	-0.077(5)	-0.32(6)	-0.066	0.080
$Q(3^+, 0)$	-	-4.9			
$\mu(1^+, 0)$	0.822	0.839(2)	0.800(1)	0.843	0.843
$\mu(3^+, 0)$	-	1.866(2)			
$B(E2; 3^+, 0)$	10.7(8)	6.1	11.65(13)		
$B(E2; 2^+, 0)$	4.4(23)	7.5	8.66(47)		
$B(M1; 0^+, 1)$	15.43(32)	14.2(1)	15.02(11)		
$B(M1; 2^+, 0)$	-	< 0.001	0.002(1)		
$B(M1; 2^+, 1)$	0.1 (3)	0.05(1)			
M_{GT}	2.170	2.227(2)	2.18(3)		

TABLE I: Selected ${}^6\text{Li}$ observables calculated up through $N_{\text{max}} = 16$. The energies are in MeV; the RMS point-proton radius is in fm; the quadrupole moments are in $e\text{fm}^2$; the magnetic moments are in μ_N ; the reduced $B(E2)$ transition probabilities are in $e^2\text{fm}^4$; and the reduced $B(M1)$ transition probabilities are in μ_N^2 . All listed transitions are to the ground state. The energies are obtained from extrapolations to the infinite basis space, with error estimates as discussed in the text; the dipole observables as well as the gs quadrupole moment are converged within the quoted uncertainty; the other quadrupole observables and the RMS point-proton radius are evaluated at $\hbar\Omega = 12.5$ MeV. We used Ref. [21] for the experimental value of the RMS radius and Ref. [26] for GT matrix element; the other experimental values are from Refs. [27, 28]. AV18/IL2 results are from Refs. [11, 29–31] and include meson-exchange corrections for the dipole observables; CD-Bonn and INOY results are from Ref. [32] calculated at $N_{\text{max}}=16$ and $\hbar\Omega=11$ and 14 MeV respectively, with the INOY gs energy extrapolated to the infinite basis space.

error estimate based on this $\hbar\Omega$ dependence.

In general, magnetic dipole observables tend to converge rapidly. Indeed the magnetic moments of the gs and first excited state, as well as the $B(M1)$ transitions to the gs, are well converged, with, at $N_{\text{max}} = 16$, a residual dependence on the basis space parameters that is of the same order as the overall accuracy of our lowest eigenvalue.

For the RMS point-proton radius, as well as the $B(E2)$ transitions to the gs, we list our results from the largest basis space, $N_{\text{max}} = 16$, at $\hbar\Omega = 12.5$ MeV, as discussed above. The electric quadrupole moment of the gs is in excellent agreement with the experimental value - perhaps better than might be expected due to basis space limitations and long-range nature of the quadrupole moment operator.

Both the gs binding energy and the excitation energies calculated with JISP16 compare favorably to those calculated with alternative realistic NN interactions, i.e. Argonne V18, CD-Bonn, INOY, and SRG evolved N3LO interactions [25, 30, 32, 33]. However, with the addition of appropriate three-body interactions, such as Illinois-2 [30, 31] or chiral three-body forces [34–36], one can obtain somewhat better agreement with data than with the NN-only interaction JISP16.

The obtained RMS point-proton radius is similar to that obtained with CD-Bonn: both are about 10% too small compared to experiment. INOY [32] gives an even smaller radius, whereas AV18 plus Illinois-2 leads to a radius [31] that is closer to the experimental value. Note however that the gs quadrupole moment obtained with that interaction is significantly larger than experiment [31].

Also the calculated magnetic moment and reduced M1 transition probabilities with JISP16 compare well with available experimental data for all the cases shown in Table I.

The $(0^+, 1)$ excited state of ${}^6\text{Li}$ is the isobaric analog of the ground state of ${}^6\text{He}$, and can be used to calculate the Gamow–Teller transition between ${}^6\text{Li}$ and ${}^6\text{He}$. Assuming isospin symmetry, the Gamow–Teller matrix element M_{GT} is to good approximation given by

$$M_{\text{GT}} = \sum_{\alpha, \beta} \rho_{\beta\alpha}^{fi} \langle \alpha | \sigma \tau_+ | \beta \rangle \quad (21)$$

and is related to the half-life [26] through

$$|M_{\text{GT}}|^2 = \frac{1}{\frac{f_A}{f_V} g_A^2} \frac{2\pi^3 \ln 2 / (G^2 |V_{ud}|^2)}{(fT_{1/2})_t m_e^5} \quad (22)$$

where $g_A = 1.2695(29)$ is the axial constant, $\frac{f_A}{f_V} = 1.00529$ accounts for the difference in the statistical rate function of the vector and axial-vector transitions, m_e is the mass of the electron, $G = 1.166371(6) \cdot 10^{-11} \text{MeV}^{-2}$ is the Fermi coupling constant, and $V_{ud} = 0.9738(4)$ is the CKM matrix element that mixes the quarks involved in the decay. Our M_{GT} result, presented in Table I, compares quite well to that calculated in [26] using the hyperspherical-harmonic expansion method with the same (JISP16) interaction; they also obtained a value of $M_{\text{GT}} = 2.227$. It is interesting to note that Ref. [26] found the exchange current corrections to the GT matrix element to be of the order of a few percent. Ref. [26] also presents the extrapolated gs binding energy of ${}^6\text{Li}$ with JISP16 as 31.46(5) MeV which is in excellent agreement of our 31.49(3) MeV result presented in Table I.

B. Density distributions

A closer look at the 3-dimensional one-body densities, free of spurious cm effects, would help to develop a physical intuition for the *ab initio* structure of a nucleus. Although it is easier to perform the deconvolution of the

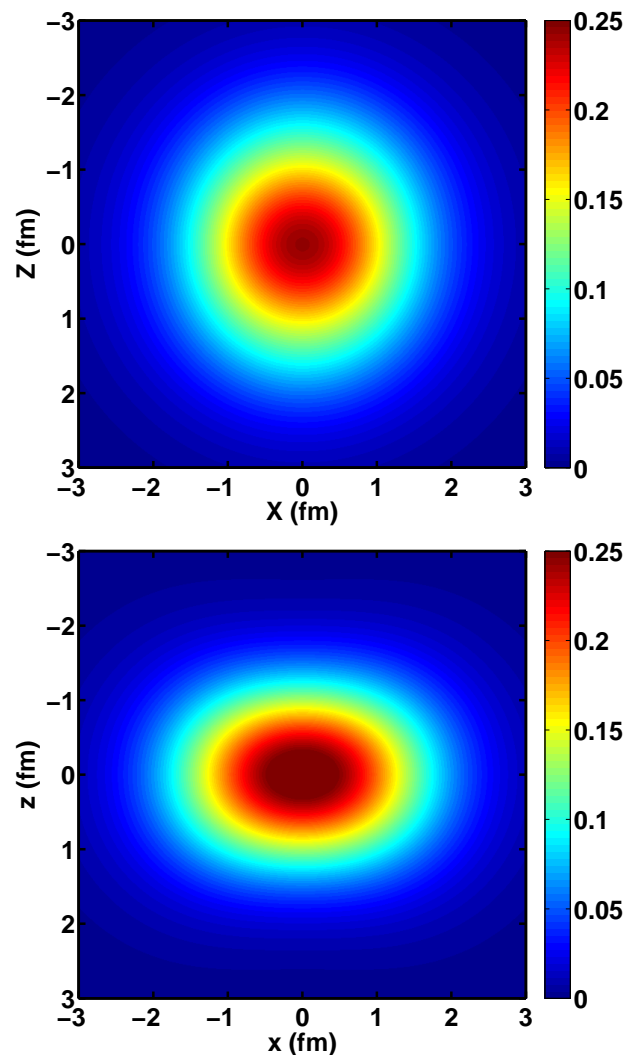


FIG. 5: (Color online) The $y = 0$ slice of the translationally-invariant matter density in the x - z plane for the gs of ${}^6\text{Li}$ (top, $J = 1$) is contrasted with the density for the first excited state (bottom, $J = 3$). These densities were calculated at $N_{\text{max}} = 16$ and $\hbar\Omega = 12.5$ MeV.

cm density after integrating out all angle-dependence one can also deconvolute the full 3-dimensional density (see the appendix for details). However, a detailed investigation of the numerical convergence is impractical for these 3-dimensional densities. We therefore present all our 3-dimensional density distributions in the largest basis space at $\hbar\Omega = 12.5$ MeV only, where the RMS radius, as well as the quadrupole moments (which are closely related to the shape of the wavefunction), appear to be reasonably converged.

In order to produce the density that represents the actual shape of a specific state of a nucleus in a translationally-invariant (inertial) frame, we set $M_J = J$ for all our calculations of the local density. That is, we select the maximal positive angular momentum projection along the axis of quantization, the z -axis. This seems

like the natural choice since the quadrupole moment Q is defined as the E2 matrix element at $J = M_J$ (or equivalently, to the reduced E2 matrix element). Note that even though we calculate 3-dimensional density distributions, our results are symmetric under rotations around the z -axis: the wavefunctions have azimuthal symmetry.

Fig. 5 shows the matter density for the lowest two states of ${}^6\text{Li}$. Both states are oblate, though the $(1^+, 0)$ state is nearly spherical whereas the $(3^+, 0)$ state is strongly oblate. Indeed, the relative deformation of the translationally-invariant densities for the gs and first excited state is implied by the results in Table I for their respective quadrupole moments. The gs has a negative calculated quadrupole that is near zero, in close agreement with experiment. On the other hand, the first excited state has a large negative calculated quadrupole moment.

It is worth commenting that our use of the terms “prolate” and “oblate” characterize the shapes in the inertial frame, not a body-fixed axis as is common for discussions of shapes in the collective model [19]. In the inertial frame of reference positive quadrupole moments correspond to prolate shapes and negative quadrupole moments correspond to oblate shapes.

Fig. 6 illustrates the effect of M_J on the density distribution as we see the oblate shape of the density at $M_J = 3$ (top panel) morph into the prolate shape at $M_J = 0$ (bottom panel). Calculating the density when $J \neq M_J$ gives a density whose azimuthal symmetry axis is not aligned with the spin. E.g. at $M_J = 0$ the symmetry axis lies in the x - y plane, perpendicular to the z -axis. The oblate shape we found at $M_J = 3$ is now also perpendicular to the z -axis. On the other hand, we do have an azimuthal symmetry around the z -axis. Therefore, what we obtain is an oblate shape perpendicular to the z -axis, but with its principle axis (symmetry axis) averaged over all directions in the x - y plane. This results in a prolate shape at $M_J = 0$, as we see in the bottom panel of Fig. 6. Note that we see the same for e.g. the E2 matrix element: with $M_J = 0$, the E2 matrix element for this state is positive, but the corresponding quadrupole moment, shown in Table I, is negative (and independent of M_J).

C. ${}^7\text{Li}$

For ${}^7\text{Li}$ we evaluated the low-lying states in basis spaces up to $N_{\text{max}} = 14$. We only consider isospin $\frac{1}{2}$ states – the lowest isospin $\frac{3}{2}$ has more than 10 MeV excitation energy. The lowest five states in the excitation energy spectrum compare well with experiment and the correct level ordering is preserved as shown in Fig. 7. The excitation energy of four of these five states shows rapid numerical convergence with N_{max} and stability with respect to variations in the HO energy. However, the convergence of the lower of the two $\frac{5}{2}^-$ states is significantly slower. Indeed, experimentally this state has a

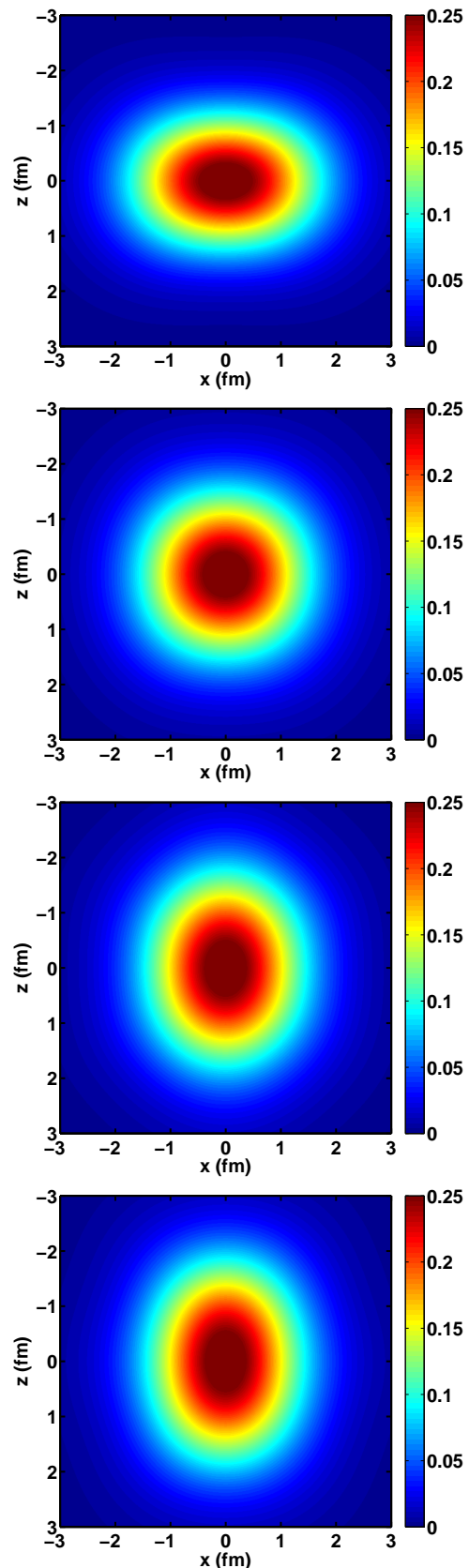


FIG. 6: (Color online) The $y = 0$ slice of the translationally-invariant matter density in the x - z plane for first excited 3^+ state of ${}^6\text{Li}$ with $M_J = 3, 2, 1, 0$ from top to bottom.

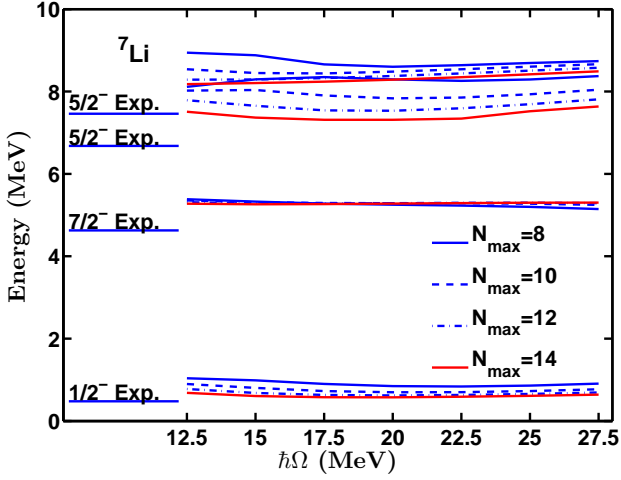


FIG. 7: (Color online) Excitation energies for selected excited states of ${}^7\text{Li}$ are shown as a function of $\hbar\Omega$ at various N_{max} values as indicated in the legend, and compared to experiment.

large width of 0.88 MeV, whereas the width of the other states is less than 0.1 MeV. Thus, as in ${}^6\text{Li}$, we again observe a good correlation between experimental width and convergence rate of excitation energies.

Our results with JISP16 for selected spectral and other observables of ${}^7\text{Li}$ are summarized in Table II and compared with experiment when available. The error estimates for the excitation energies are calculated as discussed above. From this table we see that the gs energy is underbound by about 0.67 MeV. The gs energy and excitation energies compare favorably to other methods and interactions [30, 37]. For the RMS radius and the quadrupole observables (which are not converged) we list our results from the largest basis space, $N_{\text{max}} = 14$, at $\hbar\Omega = 12.5$ MeV; they are in reasonable agreement with the available experimental data, given the basis space limitations and long-range nature of these operators.

Fig. 8 displays the magnetic dipole moments and reduced magnetic dipole transition probabilities to the gs for selected states of ${}^7\text{Li}$. These observables converge quickly, and for calculations at $N_{\text{max}} = 14$, are almost independent the HO energy. In fact, most of the magnetic observables are already reasonably well converged (to within 10%) at $N_{\text{max}} = 8$, with the noticeable exception of the two $\frac{5}{2}^-$ excited states. This is partially due to a strong state mixing between these two states. We require larger basis spaces to fully differentiate these states, because they are close together in energy, and their quantum numbers are identical.

Our estimate for the infinite basis space results for magnetic dipole observables is based on the residual dependence on N_{max} and $\hbar\Omega$ over a 10 MeV window in $\hbar\Omega$. This window does include the optimal $\hbar\Omega$ for the extrapolations and the variational upperbound, but is not necessarily centered around these values. Our numerical error estimate is the RMS sum of the variation with $\hbar\Omega$

${}^7\text{Li}$	Expt.	JISP16	AV18/IL2	CD-B	INOY
$E_b(\frac{3}{2}^-)$	39.244	38.57(4)	38.9(1)	35.56	39.6(4)
$\langle r_{pp}^2 \rangle^{1/2}$	2.30(5)	2.2	2.25(1)	2.22	2.05
$E_x(\frac{1}{2}^-)$	0.477	0.52(6)	0.2(1)		
$E_x(\frac{7}{2}^-)$	4.630(1)	5.25(5)	4.9(1)		
$E_x(\frac{5}{2}_1^-)$	6.680(50)	7.1(2)	6.6(1)		
$E_x(\frac{5}{2}_2^-)$	7.460(10)	8.1(1)	7.2(1)		
$Q(\frac{3}{2}^-)$	-4.06(8)	-3.2	-3.6(1)	-3.20	-2.79
$Q(\frac{7}{2}^-)$	-	-5.0			
$Q(\frac{5}{2}_1^-)$	-	-6.0			
$Q(\frac{5}{2}_2^-)$	-	2.3			
$\mu(\frac{3}{2}^-)$	3.256	2.954(5)	3.168(13)	3.01	3.02
$\mu(\frac{1}{2}^-)$	-	-0.76(1)			
$\mu(\frac{7}{2}^-)$	-	3.3(1)			
$\mu(\frac{5}{2}_1^-)$	-	-0.90(2)			
$\mu(\frac{5}{2}_2^-)$	-	-0.39(5)			
$B(E2; \frac{1}{2}^-)$	15.7(10)	10.2	16.2(5)		
$B(E2; \frac{7}{2}^-)$	3.4	5.1	9.92(14)		
$B(E2; \frac{5}{2}_1^-)$	-	1.5			
$B(E2; \frac{5}{2}_2^-)$	-	< 0.1			
$B(M1; \frac{1}{2}^-)$	4.92(25)	3.89(2)	4.92(7)		
$B(M1; \frac{5}{2}_1^-)$	-	0.002(1)			
$B(M1; \frac{5}{2}_2^-)$	-	0.02(1)			

TABLE II: Selected ${}^7\text{Li}$ observables calculated up through $N_{\text{max}} = 14$, with the same units as in Table I. The energies are obtained from extrapolations to the infinite basis space, and the magnetic dipole observables are nearly converged, with error estimates as discussed in the text; the RMS point-proton radius and electric quadrupole observables are evaluated at $\hbar\Omega = 12.5$ MeV. Experimental values are from Refs. [21, 27, 28]. AV18/IL2 results are from Refs. [11, 29–31] and include meson-exchange corrections for the dipole observables; CD-Bonn and INOY results are from Ref. [32], and were calculated at $N_{\text{max}}=12$ and $\hbar\Omega=11$ and 16 MeV respectively for CD-Bonn and INOY, with the INOY gs energy extrapolated to the infinite basis space.

over this window and the difference between the results in the two largest N_{max} calculations (rounded up), i.e. treating the variation with each of the two basis space parameters as independent sources of numerical uncertainties.

With JISP16, the magnetic moment of the gs is about 10% too low compared to experiment. This could easily arise from our neglect of meson-exchange currents in our current calculations. GFMC calculations with AV18 plus Illinois-2 three-body forces [11] found that the magnetic moment of the ${}^7\text{Li}$ gs receives a 10% correction from meson-exchange currents, changing the magnetic moment from $2.9 \mu_N$ to $3.2 \mu_N$. It is quite remarkable that our result for the magnetic moment, with the naive pointlike M1 operator, is in fact quite close to the results

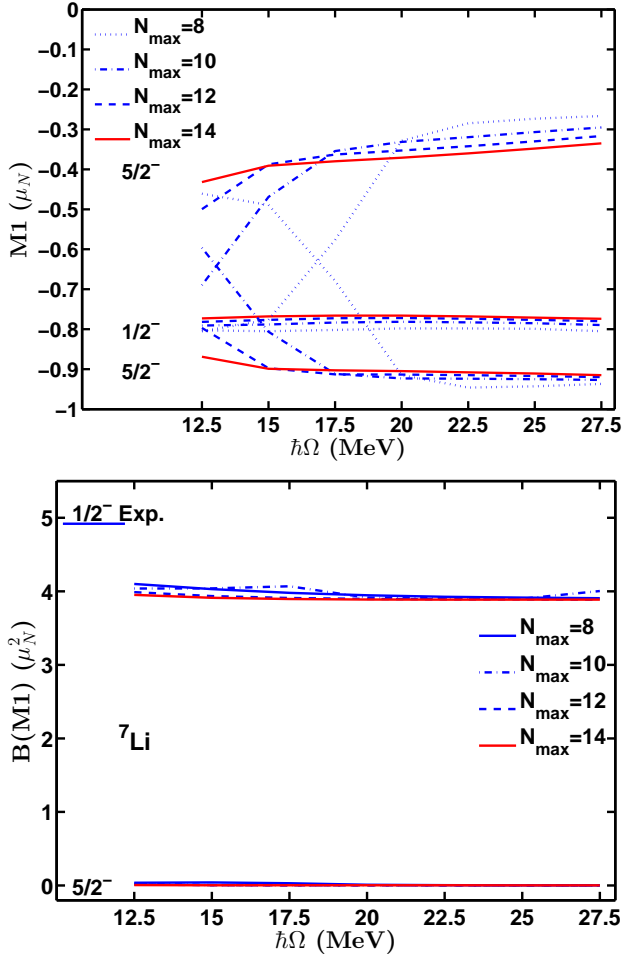


FIG. 8: (Color online) Dipole moment (top) and $B(M1)$ transition to the gs (bottom) as a function of the basis $\hbar\Omega$ for selected excited states of ${}^7\text{Li}$ at various N_{\max} values as indicated in the legend. The experimental value for the $B(M1)$ transition from the excited $1/2^-$ to the ground state is indicated on the left side of the lower panel and is about 20% larger than the theoretical result.

obtained with CD-Bonn, with INOY, and with AV18 plus Illinois-2, all about 10% below the experimental datum. Apparently, this observable is not very sensitive to the details of the interaction. (Note that the exchange current correction to the ${}^6\text{Li}$ gs magnetic moment was only 2% in Ref. [11].)

The $B(M1)$ from the $1/2^-$ to the gs is about 20% too low compared to experiment. Again, this is in qualitative agreement with the findings of Ref. [11]: with AV18 plus Illinois-2 there is about 10% increase in the $M1$ transition matrix element due to meson-exchange currents, which results in a 20% increase in the corresponding $B(M1)$.

The effect of the cm motion on the density is shown in Fig. 9 for the gs of ${}^7\text{Li}$. The top panel shows the space-fixed (sf) density including the cm motion, $\rho_{\text{sf}}^\Omega(\vec{r})$, whereas the bottom panel shows the translationally-

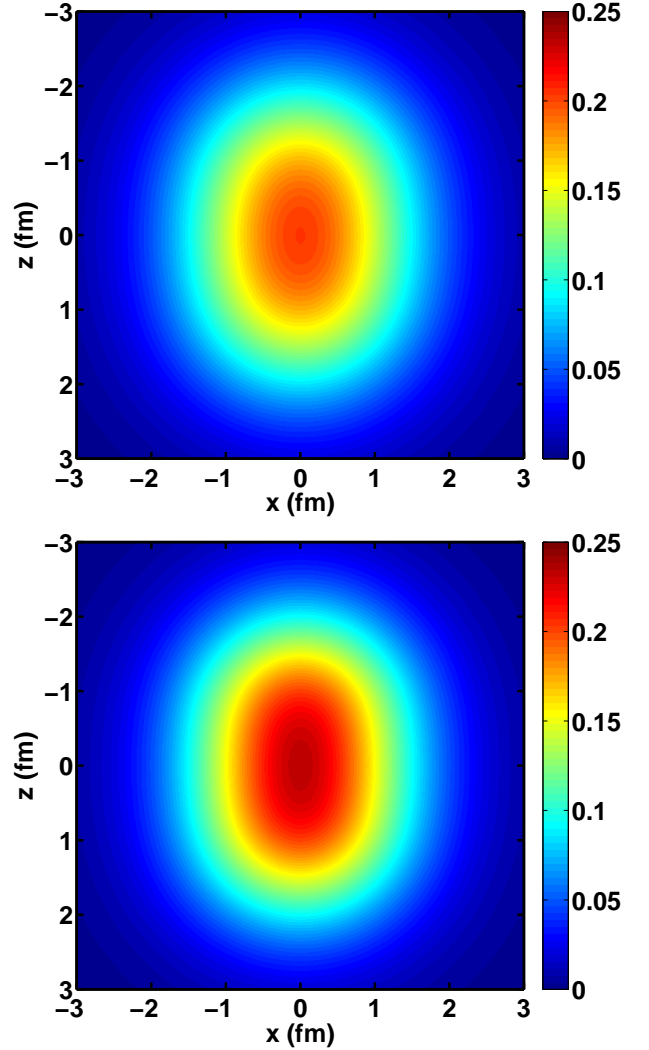


FIG. 9: (Color online) The $y = 0$ slice of the gs matter density of ${}^7\text{Li}$ before (top) and after (bottom) deconvolution of the spurious cm motion. These densities were calculated at $N_{\max} = 14$ and $\hbar\Omega = 12.5$ MeV.

invariant density, $\rho_{\text{ti}}(\vec{r})$. The smearing of the density due to the cm motion leads to a diminished central density; the sf density has a central value of 0.204 nucleons/fm³ while the ti density has a central value of 0.233 nucleons/fm³.

The cm motion smearing spreads out the sf density leading to a slower falloff and a larger radius than the ti density. Furthermore, the ti density has a more pronounced oblate shape than the sf density, as would be expected from smearing with a spherically-symmetric function that averages out the non-spherical details. In order to characterize the degree of deformation, we compare the ratio of the long axis to the short axis of the elliptical density slices. The ratio of the long to short axes at half central density is 1.78 for the ti density and 1.60 for the sf density. Note that the extent of the smearing effect from cm motion depends on the HO energy of the

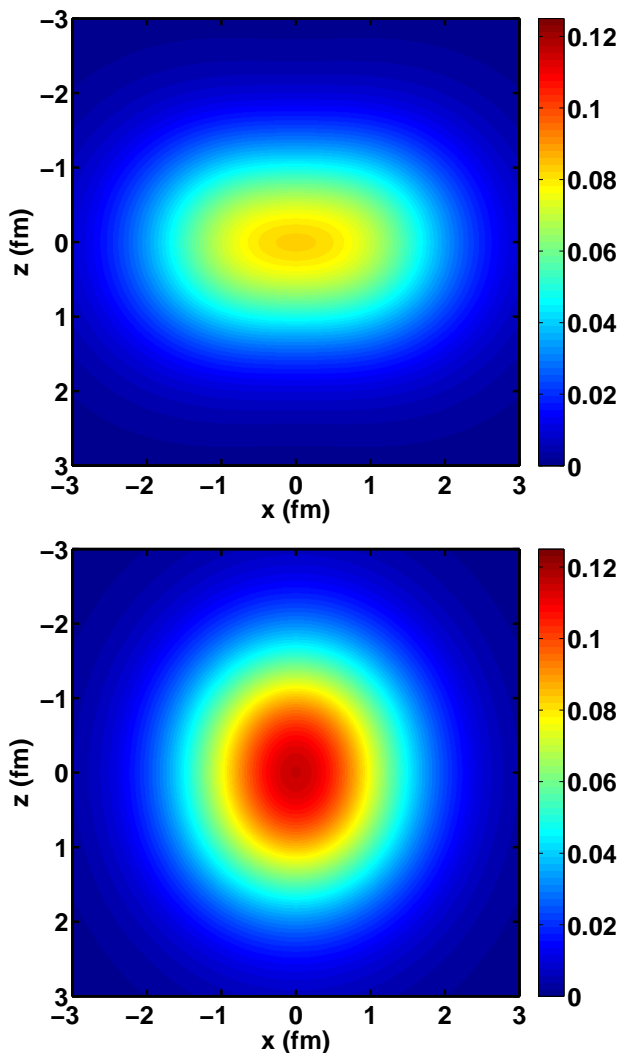


FIG. 10: (Color online) The $y = 0$ slices of the translationally-invariant proton densities for the first excited $\frac{5}{2}^-$ state (top) and for the second excited $\frac{5}{2}^-$ state (bottom) of ${}^7\text{Li}$. These densities were calculated at $N_{\text{max}} = 14$ and $\hbar\Omega = 12.5$ MeV.

basis. The sf density depends on $\hbar\Omega$, even in the limit $N_{\text{max}} \rightarrow \infty$, whereas the ti density becomes independent of the basis in this limit.

Fig. 10 contrasts proton densities of the fourth and fifth excited states of ${}^7\text{Li}$. Although their quantum numbers are equal, $(J^\pi, T) = (\frac{5}{2}^-, \frac{1}{2})$, they have other features that make them quite distinct. Experimentally, the first excited $\frac{5}{2}^-$ is broad, whereas the second excited $\frac{5}{2}^-$ is narrow: their widths are 0.88 MeV and 0.09 MeV respectively. Indeed, our calculated excitation energy is better converged for the higher of these two states. Furthermore, our calculations show significant differences in their structure: the first excited $\frac{5}{2}^-$ has a large negative quadrupole moment, whereas the second has a moderate positive quadrupole moment (see Table II). Indeed, the density in the top panel of Fig. 10 is strongly oblate,

${}^8\text{Li}$	Expt.	JISP16	AV18/IL2	CD-B	INOY
$E_b(2^+)$	41.277	40.3(2)	41.9(2)	35.82	41.3(5)
$\langle r_{pp}^2 \rangle^{1/2}$	2.21(6)	2.1	2.09(1)	2.17	2.01
$E_x(1^+)$	0.981	1.5(2)	1.4(3)		
$E_x(3^+)$	2.255(3)	2.8(1)	2.5(3)		
$E_x(4^+)$	6.53(2)	7.0(3)	7.2(3)		
$Q(2^+)$	3.27(6)	2.6	3.2(1)	2.78	2.55
$Q(1^+)$	-	1.2			
$Q(3^+)$	-	-2.0			
$Q(4^+)$	-	-3.4			
$\mu(2^+)$	1.654	1.3(1)	1.65(1)	1.24	1.42
$\mu(1^+)$	-	-2.2(2)			
$\mu(3^+)$	-	2.0(1)			
$\mu(4^+)$	-	1.84(1)			
$B(E2;1^+)$	-	1.9			
$B(E2;3^+)$	-	4.6			
$B(E2;4^+)$	-	1.9			
$B(M1;1^+)$	5.0(16)	3.7(2)			
$B(M1;3^+)$	0.52(23)	0.25(5)			

TABLE III: Selected ${}^8\text{Li}$ observables calculated up through $N_{\text{max}} = 12$, with the same units as in Table I. The energies are obtained from extrapolations to the infinite basis space, and the magnetic dipole observables are nearly converged, with error estimates as discussed in the text; the RMS point-proton radius and electric quadrupole observables are evaluated at $\hbar\Omega = 12.5$ MeV. Experimental values are from Refs. [21, 38, 39]. AV18/IL2 results are from Refs. [30, 31] and does not include meson-exchange corrections for the magnetic moment; CD-Bonn and INOY results are from Ref. [32], and were calculated at $N_{\text{max}}=12$ and $\hbar\Omega=12$ and 16 MeV respectively for CD-Bonn and INOY, with the INOY gs energy extrapolated to the infinite basis space.

whereas the bottom panel shows a moderately prolate shape (we note again that the densities are symmetric around the azimuthal axis, which is the vertical axis in these plots). Another noteworthy difference is observed in the magnitude of the central proton density: the more diffuse $(\frac{5}{2}^-, \frac{1}{2})_1$ state has a central proton density of only 0.08 protons/ fm^3 while the $(\frac{5}{2}^-, \frac{1}{2})_2$ state has a central proton density of 0.12 protons/ fm^3 , 50% higher.

D. ${}^8\text{Li}$

Table III presents a capsule view of selected spectral and other observables for ${}^8\text{Li}$ calculated with JISP16 and compared with experiment when available. The error estimates for the excitation energies and magnetic dipole observables are calculated as discussed above. For the RMS point-proton radius and the charge quadrupole observables (which are not converged) we list our re-

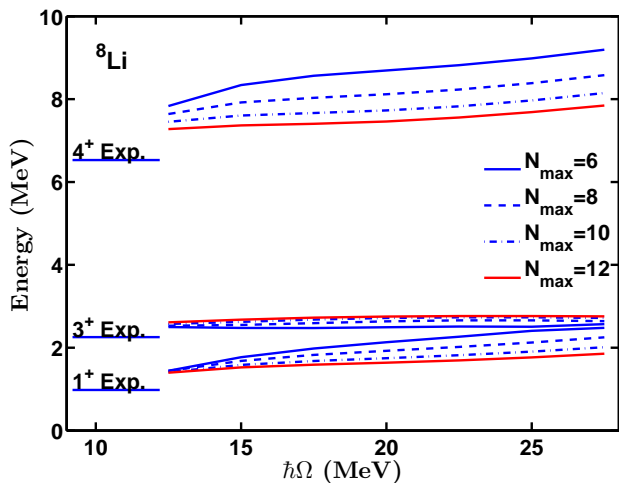


FIG. 11: (Color online) Excitation energies for select excited states of ${}^8\text{Li}$ are shown as a function of $\hbar\Omega$ at various N_{max} values as indicated in the legend.

sults from the largest basis space, $N_{\text{max}} = 12$, at $\hbar\Omega = 12.5$ MeV. From this table we see that the gs energy is underbound by about 1.0 MeV.

In addition to the gs, we examined several narrow low-lying states: the lowest two excited states, which are narrow states, with a width of 33 keV or less, as well as a narrow low-lying 4^+ state at 6.53 MeV with a width of 35 keV. We do not consider isospin 2 states – the lowest isospin 2 has more than 10 MeV excitation energy. The excitation energies obtained with JISP16 compare reasonably well with the experimental excitation energies, though the level splittings are a bit too large (see Fig. 11). The convergence of the spectrum is similar as for the other Li-isotopes, though the convergence of the 4^+ state is somewhat slower than expected based on its small width. In our calculations there are several additional states below this 4^+ state, which is typically the 8th state in our calculated spectrum, depending on the basis space; experimentally, it is the 7th observed state.

The convergence properties of the calculated magnetic dipole observables are similar to those for ${}^6\text{Li}$ and ${}^7\text{Li}$ discussed above. Because we can only go up to $N_{\text{max}} = 12$, the numerical error estimates are slightly larger than for ${}^6\text{Li}$ and ${}^7\text{Li}$. The gs magnetic moment is approximately 20% lower than experiment. This seems reasonable, in light of our discussions of magnetic moments above, that this discrepancy is at least partially due to the fact that we do not incorporate meson-exchange currents.

Note that CD-Bonn gives a similar magnetic moment as JISP16, but that INOY provides a moment that is slightly closer to experiment, and AV18/IL2 gives a magnetic moment in excellent agreement with data; however, the contributions of meson-exchange currents were not evaluated for this magnetic moment.

The reduced $B(M1)$ transition probabilities from the 1^+ and 3^+ to the gs are 20% and 50% lower than ex-

periment, but the experimental error bars are large. The magnetic moment of the 4^+ state is remarkably well converged, despite its excitation energy not being very well converged.

The quadrupole moments and reduced $B(E2)$ transition probabilities are not well converged due to basis space limitations, as discussed above. In spite of these limitations, the electric quadrupole moments allow us to qualitatively understand the shape of the proton densities of these states: prolate for the 2^+ gs and the first excited 1^+ , but oblate for the first excited 3^+ and 4^+ states. Indeed, that is what we see in the left-hand panels of Fig. 12, where we plot these densities for the gs and for the 4^+ state.

Interestingly, the neutron density differs by more than a simple scale change from the proton density for these two states, as can be seen from the right-hand panels of Fig. 12. In the 2^+ state, the deformation of the neutrons is significantly larger than that of the protons, whereas in the 4^+ state, the deformation of the neutrons is much smaller than that of the protons.

A case of special interest can be seen in the top right panel of Fig. 12, or in more detail in Fig. 13. In the left panel of Fig. 13 we clearly see non-trivial neutron clustering that is obfuscated in the sf frame (right), highlighting the importance of the deconvolution procedure and the significance of the ti density. Furthermore, the ti density (left panel) has a significantly higher density in the central region than the sf density (right panel). Both the ti and the sf densities are normalized to give the same integrated density of five neutrons, so that means that the sf density is smeared out over a larger region, and falls off to zero slower than the ti density. This is also evident in Fig. 9, where we contrasted the sf and ti matter density of the gs of ${}^7\text{Li}$: the ti central density is significantly higher than the sf central density.

Another way of visualizing these ti densities is by plotting their multipole components, $\rho^{(K)}(r)$ (we omit the “ti” subscript for compactness of notation). In order to exhibit their long distance features, we present the magnitudes of the $\rho^{(K)}(r)$ in Fig. 14 for the 2^+ gs and the first excited 4^+ state of ${}^8\text{Li}$ as semilog plots out to a radius of 6 fm. To illustrate the radial and angular nodal structure together out to 4 fm, we present in Fig. 15 the $y = 0$ slices of the multipole components for the gs proton density (left panels) and gs neutron density (right panels) defined as their full contribution to the total density. That is, Fig. 15 displays slices of the respective full terms contributing to the sum given in Eq. (10). Hence, the sum of the proton (neutron) multipoles in Fig. 15 produces the top left (top right) panel of Fig. 12 out to 4 fm.

Let us consider Fig. 14 in more detail. Qualitatively, the multipole components look very similar for the gs protons and gs neutrons. The main difference seems to be that the proton densities fall off more rapidly with r than the neutron densities for all three multipole components. This is understandable since this is a neutron-rich system

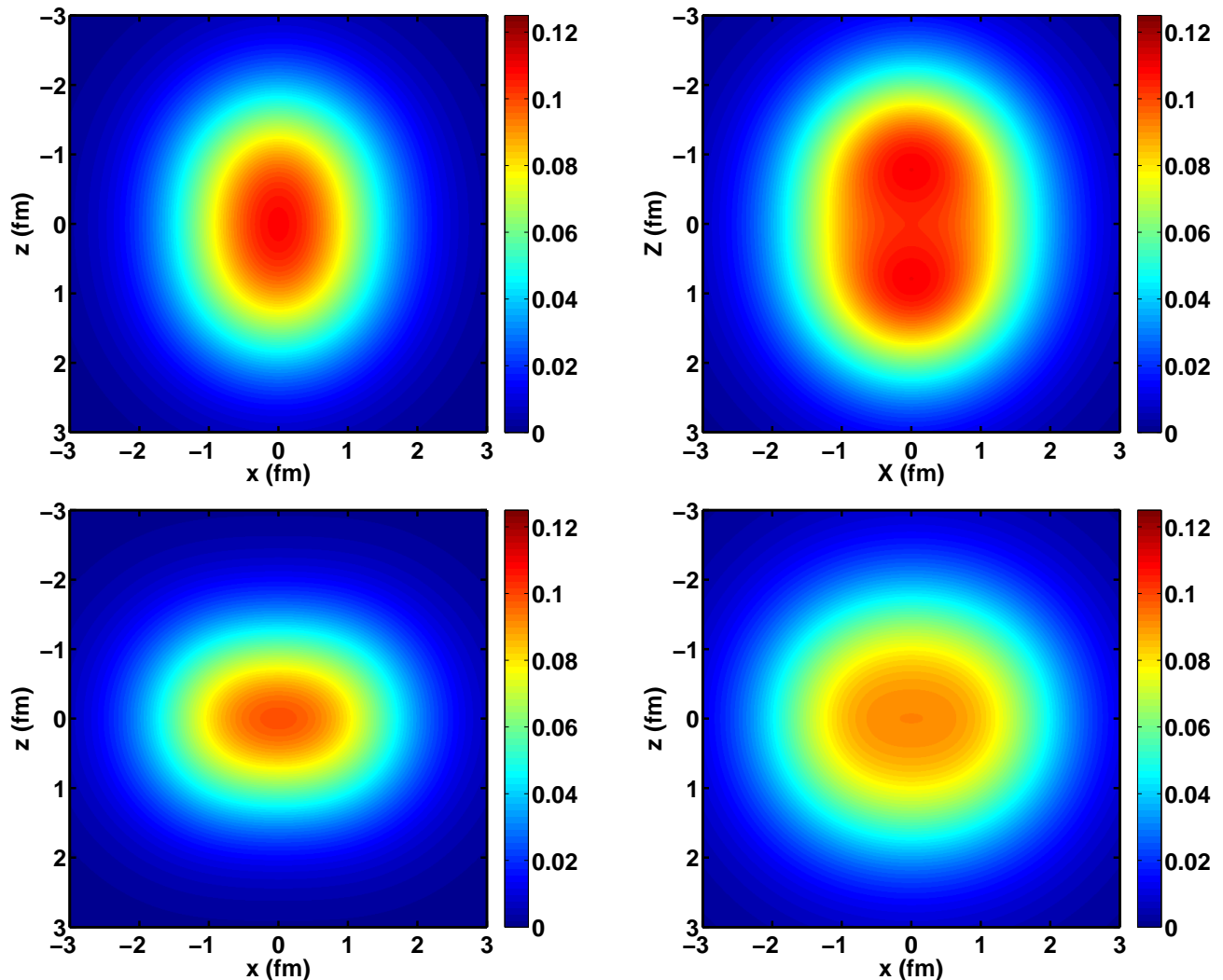


FIG. 12: (Color online) The $y = 0$ slice of the translationally-invariant proton (left) and neutron (right) densities of the 2^+ gs (top) and the first excited 4^+ state (bottom) of ${}^8\text{Li}$. These densities were calculated at $N_{\text{max}} = 12$ and $\hbar\Omega = 12.5$ MeV.

and the single-neutron removal energy is less than that of the single-proton removal energy. Note however that the clustering of the neutrons in the gs of ${}^8\text{Li}$ (left panel of Fig. 13) is not evident from the multipole components $\rho^{(K)}$ of the neutron density displayed in the top right panel of Fig. 14. That is, even though the radial multipole densities of the protons and neutrons look qualitatively similar, the corresponding 3-dimensional densities look qualitatively different. Apart from overall difference in the asymptotic behavior, the biggest difference between the proton and neutron multipole densities is in the interior of the nucleus, below 2.5 fm, where the magnitude of the proton hexadecapole density is up to 60% larger than that of the neutron hexadecapole density. On the other hand, in the exterior region, beyond 4 fm, the neutron hexadecapole density is more than an order of magnitude larger than the proton density.

The monopole proton and neutron densities of the first excited 4^+ state of ${}^8\text{Li}$ seen in Fig. 14 are similar to those

of the ground state, with the proton density falling off more rapidly than the neutron density. On the other hand, the higher multipole components $\rho^{(K)}(r)$ of the first excited 4^+ state of ${}^8\text{Li}$ look qualitatively quite different than those of the ground state. In addition, the protons and the neutrons of the excited 4^+ state differ from each other in their higher multipole components. The quadrupole density of the neutrons in the 4^+ state has a node, in contrast to that of the protons. Neither the proton nor the neutron hexadecapole density has a node in the 4^+ state, whereas both the proton and the neutron hexadecapole densities have a node in the ground state.

We turn our attention now to the nodal structures of the multipole components of the charge-dependent density distributions for the gs of ${}^8\text{Li}$ in Fig. 15. Since each panel represents a term contributing to Eq.(10), we observe the angular nodal structure governed by the respective spherical harmonic factor. The radial nodes arise from the radial functions $\rho^{(K)}(r)$ displayed in Fig. 14.

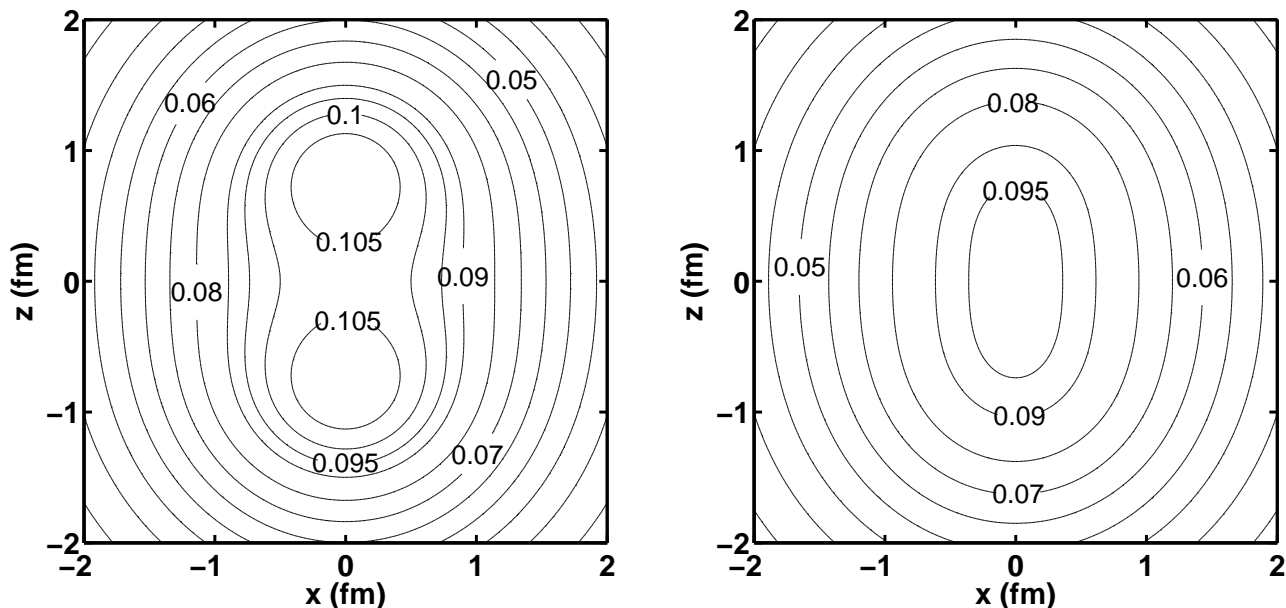


FIG. 13: (Color online) The $y = 0$ slice of the translationally-invariant neutron density (left) of the 2^+ gs of ${}^8\text{Li}$. The space-fixed neutron density for the same state is on the right. The contour labels give the density in neutrons/ fm^3 . These densities were calculated at $N_{\text{max}} = 12$ and $\hbar\Omega = 12.5$ MeV.

The significant differences between the proton and the neutron magnitudes at each multipolarity reflect the differences in the magnitudes of the radial distributions of the multipoles seen above in the top two panels of Fig. 14.

From both Figs. 14 and 15, one observes that the gs proton monopole density has a slightly higher central value than the neutron gs monopole density, but it falls off much more rapidly with r than the neutron density. On the other hand, the gs neutron quadrupole density has larger (in magnitude) features than the gs proton density, both at small and large distances. And again, the gs hexadecapole densities have the most interesting features, including the nodal structure at about 3 fm. In the interior region of the nucleus, the gs proton hexadecapole density has more pronounced features, whereas in region beyond 3 fm the gs neutron hexadecapole density has more pronounced features. However, none of these multipole density plots show any hint of clustering of the neutrons; nevertheless, the plots of the three gs neutron multipole densities of Fig. 15 add up to give the total translationally-invariant density of the left panel of Fig. 13, which does indicate two neutron clusters, with their centers separated by about 1.5 fm.

Although these densities are not (yet) fully converged, we feel that the qualitative features will persist in the limit of a complete basis. In particular salient differences between different states and/or between the proton and neutron densities are likely to survive in that limit.

IV. SUMMARY AND OUTLOOK

We have performed no-core full configuration calculations for the Lithium isotopes, ${}^6\text{Li}$, ${}^7\text{Li}$, and ${}^8\text{Li}$ with the realistic NN interaction JISP16. Several observables obtained (gs energies, excitation energies, magnetic dipole moments and reduced magnetic dipole transition probabilities) compare well with both experiment and alternate methods and interactions. For certain observables that are more sensitive to long-range correlations (the RMS radius, electric quadrupole moments, and reduced quadrupole transition probabilities) we were unable to obtain full convergence, though they also compare favorably with alternate methods and interactions.

One-dimensional and three-dimensional translationally-invariant one-body density distributions were calculated for various ground and excited states of ${}^6\text{Li}$, ${}^7\text{Li}$, and ${}^8\text{Li}$. These one-body density distributions provide an excellent framework for visualization of nuclear shape distortions and clustering effects. The associated one-body density matrix in the HO basis provides a compact form of all of the quantum one-body information for a given nuclear state.

To improve our convergence, especially for matrix elements of long-range operators, we would require significant increases in basis space sizes (increased N_{max}) and/or alternatives to the HO single-particle basis. Recent advances in the “Importance-Truncated No-Core Shell Model” [40, 41], the “Symmetry-Adapted No-Core Shell Model” [42] and the “No-Core Monte Carlo Shell Model” [43, 44] are promising new methods for accessing much larger basis spaces.

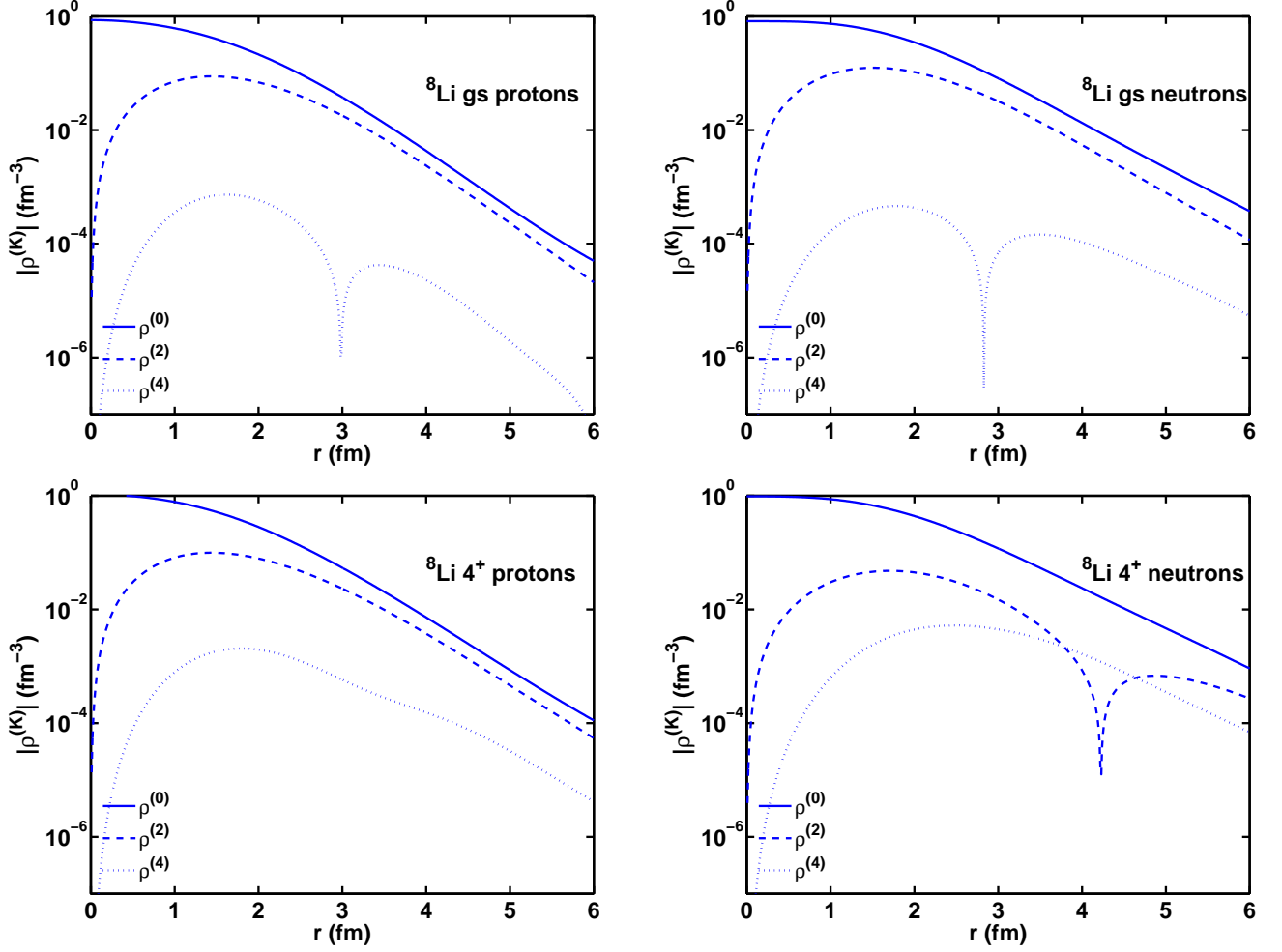


FIG. 14: (Color online) The multipole components $\rho_{ti}^{(K)}(r)$ of the proton (left) and neutron (right) densities of the 2^+ gs (top) and the first excited 4^+ state (bottom) of ${}^8\text{Li}$. These densities were calculated at $N_{\text{max}} = 12$ and $\hbar\Omega = 12.5$ MeV. Monopole and quadrupole distributions for the gs are all positive. The $K = 4$ distributions for the gs are negative in the interior and positive in the tail region. For the 4^+ state, the monopoles are positive while the quadrupole is negative for the protons and negative for the interior of the neutrons. Both $K = 4$ distributions are positive for the 4^+ state.

Further advances in NN interactions, as well as three-body forces, could also help resolve some of the residual differences between theory and experiment. Of course, there is also the possibility that four-body forces may play a significant role.

Acknowledgments

We would like to thank Mark Caprio, Michael Kruse, John Millener, and Petr Navrátil for stimulating discussions. This work was supported in part by U.S. Department of Energy Grant DE-FC02-09ER41582 (SciDAC/UNEDF) and DE-FG02-87ER40371, and by the US NSF grant 0904782. Computational resources were provided by the National Energy Research Supercomputer Center (NERSC), which is supported by the Office of Science of the U.S. Department of Energy.

Appendix A: Deconvolution of the one-body density

In our many-body framework, we use the Slater determinants of a single-particle Harmonic Oscillator (HO) basis. In this basis, we can define a space-fixed One-Body Density Matrix (OBDM) by its matrix elements

$$\rho_{\beta\alpha}^{fi} = \langle \Psi_f | a_{\alpha}^{\dagger} a_{\beta} | \Psi_i \rangle, \quad (\text{A1})$$

where α and β stand for a set of single-particle quantum numbers $(n_{\alpha}, l_{\alpha}, j_{\alpha}, m_{\alpha}, \tau_{z,\alpha})$ and $(n_{\beta}, l_{\beta}, j_{\beta}, m_{\beta}, \tau_{z,\beta})$. These matrix elements $\rho_{\beta\alpha}^{fi}$, together with the expressions for the single-particle wavefunctions $\psi_{\alpha}(\vec{r})$, completely determine the OBDM in coordinate space

$$\rho^{fi}(\vec{r}, \vec{r}') = \sum_{\alpha, \beta} \rho_{\beta\alpha}^{fi} \psi_{\alpha}^*(\vec{r}) \psi_{\beta}(\vec{r}'). \quad (\text{A2})$$

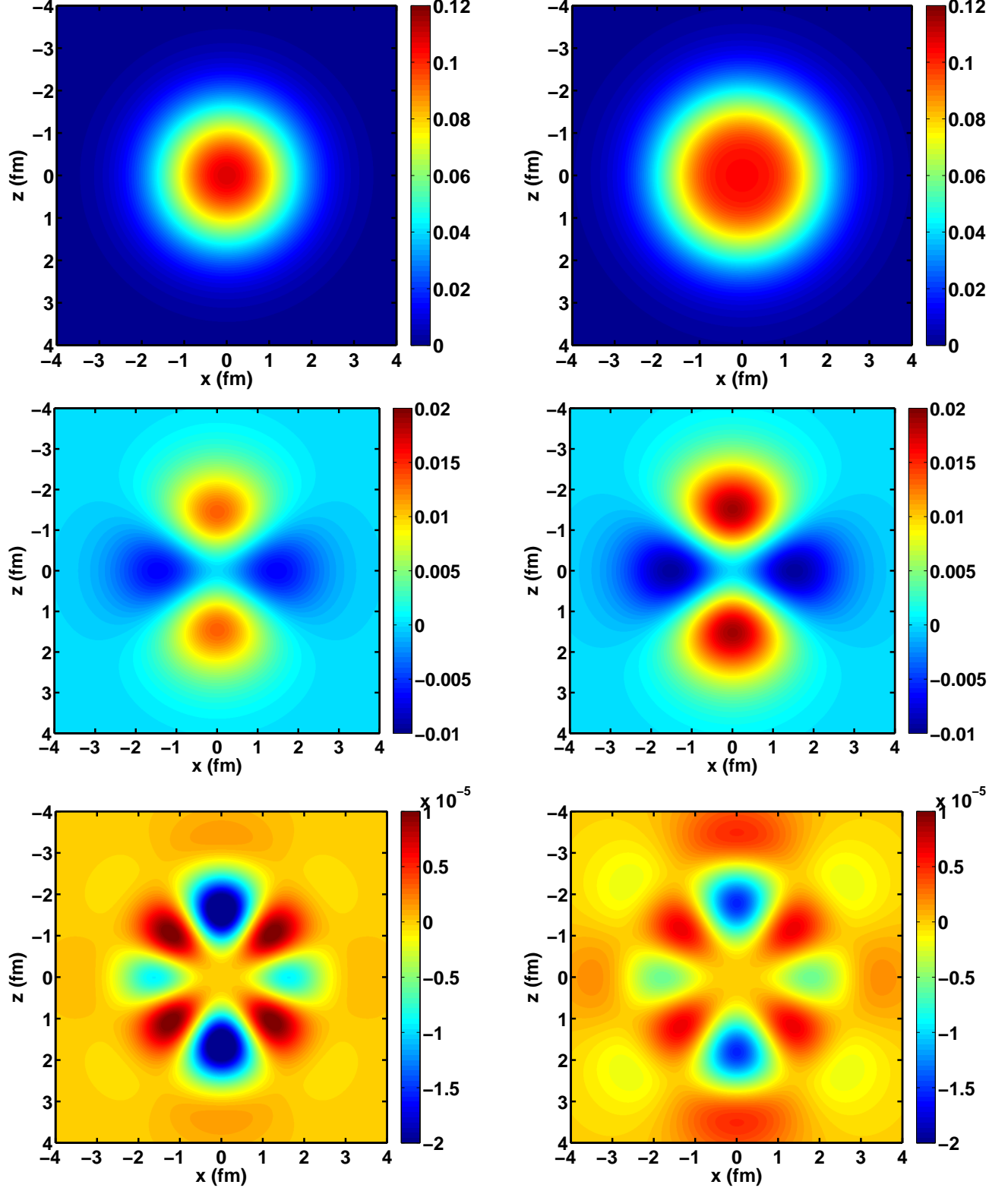


FIG. 15: (Color online) The $y = 0$ slices of the translationally-invariant proton (left) and neutron (right) densities of the 2^+ gs of ${}^8\text{Li}$. From top to bottom, we present the monopole, quadrupole and hexadecapole densities respectively. These densities were calculated at $N_{\text{max}} = 12$ and $\hbar\Omega = 12.5$ MeV.

The local one-body density becomes

$$\rho_{\text{sf}}^{\Omega}(\vec{r}) = \sum_{\alpha, \beta} \rho_{\beta\alpha} \psi_{\alpha}^*(\vec{r}) \psi_{\beta}(\vec{r}). \quad (\text{A3})$$

where

$$\begin{aligned} \psi_{\alpha}(\vec{r}) &= \langle \vec{r} | \alpha \rangle \\ &= \sum_{m_l, m_s} \langle l_{\alpha} m_l s_{\alpha} m_s | j_{\alpha} m_{j\alpha} \rangle \phi_{n_{\alpha} l_{\alpha} m_l}(\vec{r}) \\ &\quad \times \chi_{s_{\alpha} m_s} \end{aligned} \quad (\text{A4})$$

with $\phi_{n_{\alpha} l_{\alpha} m_l}(\vec{r})$ as the usual three-dimensional HO coordinate-space wavefunction and $\chi_{s_{\alpha} m_s}$ is the Pauli spinor for the nucleon. While we retain the same basis functions ψ_{α} for neutrons and for protons (subject to potentially different single-particle state cutoffs as dictated by N_{max}), our many-body states treat the neutrons and protons independently so isospin is not a conserved quantity. The one-body density distribution is normalized to the number of nucleons

$$\int \rho_{\text{sf}}^{\Omega}(\vec{r}) d^3 r = A. \quad (\text{A5})$$

This local one-body density distribution includes contributions from the cm (center of mass) motion of the many-body wavefunctions $\Psi(\vec{r}_1, \dots, \vec{r}_A)$, hence the subscript sf (space-fixed). However, because of the exact factorization of the cm wavefunction and the ti (translationally-invariant) wavefunction, the sf density can be expressed as a convolution of the ti density distribution ρ_{ti} with the cm density distribution ρ_{cm} via

$$\rho_{\text{sf}}^{\Omega}(\vec{r}) = \int \rho_{\text{ti}}(\vec{r} - \vec{R}) \rho_{\text{cm}}^{\Omega}(\vec{R}) d^3 \vec{R}. \quad (\text{A6})$$

For a HO basis, $\rho_{\text{cm}}^{\Omega}$ is a simple Gaussian (the gs density of H_{cm}) that smears out any non-spherical features of ρ_{ti} . This smearing also introduces into ρ an undesired dependence on the basis parameter $\hbar\Omega$ that could mask the convergence of ρ_{ti} . Given our expansion in a HO basis, we have analytically evaluated Eq. (A7) using our OBDMs with *Mathematica* [45]. This produces an analytic expression for the ti OBDM.

In order to display properties of the density ρ_{ti} , as well as investigate its convergence, we deconvolute the spurious cm density using well-known Fourier methods [15]. The ti density is given by

$$\rho_{\text{ti}}(\vec{r}) = F^{-1} \left[\frac{F[\rho_{\text{sf}}^{\Omega}(\vec{r})]}{F[\rho_{\text{cm}}^{\Omega}(\vec{R})]} \right] \quad (\text{A7})$$

where $F[f(\vec{r})]$ is the 3-dimensional Fourier transform of $f(\vec{r})$.

For an A -nucleon eigenstate with total angular momentum J and projection M , and possibly additional quantum numbers λ , denoted by $|A\lambda JM\rangle$, we can evaluate the local space-fixed density by evaluating the matrix

element [46] (henceforward, we omit the superscript " Ω " for compactness of notation)

$$\rho_{\text{sf}}(\vec{r}) = \langle A\lambda JM | \hat{\rho}_{\text{sf}}(\vec{r}) | A\lambda JM \rangle \quad (\text{A8})$$

using the local density operator

$$\begin{aligned} \hat{\rho}_{\text{sf}}(\vec{r}) &= \sum_{k=1}^A \delta^3(\vec{r} - \vec{r}_k) \\ &= \sum_{k=1}^A \frac{\delta(r - r_k)}{r^2} \sum_{lm} Y_l^{*m}(\hat{r}_k) Y_l^m(\hat{r}) \end{aligned} \quad (\text{A9})$$

where \hat{r} is the unit vector in the direction \vec{r} , and $Y_l^m(\hat{r})$ is a spherical harmonic. Note that it has the property

$$Y_l^{-m}(\hat{r}) = (-1)^m Y_l^{*m}(\hat{r}). \quad (\text{A10})$$

To efficiently perform the deconvolution of the spurious cm density and the ti density, we make a multipole expansion of the local density [46]

$$\rho_{\text{sf}}(\vec{r}) = \sum_K \frac{\langle JM K 0 | JM \rangle}{\sqrt{2J+1}} Y_K^{*0}(\hat{r}) \rho_{\text{sf}}^{(K)}(r) \quad (\text{A11})$$

where $\rho_{\text{sf}}^{(K)}(r)$ is the K^{th} multipole of the sf density. The same equation with "sf" replaced by "ti" provides the corresponding expansion for the local ti density. For initial and final states with spin J , the multipoles range from $K = 0$ to $K = 2J$. This multipole expansion greatly simplifies the Fourier transforms needed for the deconvolution, as we will see at the end of this appendix.

With a HO single-particle basis, each multipole is given by

$$\begin{aligned} \rho_{\text{sf}}^{(K)}(r) &= \sum R_{n_1 l_1}(r) R_{n_2 l_2}(r) \frac{-1}{\hat{K}} \langle l_1 \frac{1}{2} j_1 || Y_K || l_2 \frac{1}{2} j_2 \rangle \\ &\quad \times \langle A\lambda J || (a_{n_1 l_1 j_1}^{\dagger} \tilde{a}_{n_2 l_2 j_2})^{(K)} || A\lambda J \rangle, \end{aligned} \quad (\text{A12})$$

where $\hat{K} = \sqrt{2K+1}$. The $R_{nl}(r)$'s are the radial components of the HO wavefunction

$$R_{nl}(r) = \left[\frac{2(2\nu)^{l+3/2} \Gamma(n+1)}{\Gamma(n + \frac{l}{2} + \frac{3}{2})} \right]^{1/2} e^{-\nu r^2} L_n^{l+\frac{1}{2}}(2\nu r^2) \quad (\text{A13})$$

with $L_n^{l+\frac{1}{2}}$ the associated Laguerre polynomials and $\nu = mc^2 \hbar \Omega / (2\hbar^2 c^2)$. The reduced matrix element of a spherical harmonic in Eq. (A12) can be written as

$$\begin{aligned} \langle l_1 \frac{1}{2} j_1 || Y_K || l_2 \frac{1}{2} j_2 \rangle &= \frac{1}{\sqrt{4\pi}} \hat{j}_1 \hat{j}_2 \hat{l}_1 \hat{l}_2 \\ &\quad \times (-1)^{j_1 + \frac{1}{2}} \langle l_1 0 l_2 0 | K 0 \rangle \left\{ \begin{matrix} j_1 & j_2 & K \\ l_2 & l_1 & \frac{1}{2} \end{matrix} \right\} \end{aligned} \quad (\text{A14})$$

using a Wigner-6J coefficient. (We use the Condon-Shortley convention for the Clebsch-Gordan coefficients, defined in Ref. [18].)

Finally, $\langle A\lambda J || (a_{n_1 l_1 j_1}^\dagger \tilde{a}_{n_2 l_2 j_2})^{(K)} || A\lambda J \rangle$ in Eq. (A12) represents a reduced matrix element of the K^{th} multipole of the OBDM. The K^{th} multipole operator for initial and final states with the same M_j can be written as

$$(a_{n_1 l_1 j_1}^\dagger \tilde{a}_{n_2 l_2 j_2})^{(K)} = \sum_{m_j} (-1)^{j_2+m_j} \langle j_1 m_j j_2 - m_j | K 0 \rangle \times a_{n_1 l_1 j_1 m_j}^\dagger a_{n_2 l_2 j_2 m_j}. \quad (\text{A15})$$

Note that in Eq. (A12) we use M_j -independent reduced matrix elements, defined by the Wigner–Eckart theorem. For a generic operator T_{Kk} the reduced matrix element is defined by

$$\langle \lambda_f J_f || T_K || \lambda_i J_i \rangle = \hat{J}_f \frac{\langle \lambda_f J_f M_f | T_{Kk} | \lambda_i J_i M_i \rangle}{\langle J_f M_f K k | J_i M_i \rangle} \quad (\text{A16})$$

provided that the Clebsch-Gordan coefficient in the denominator is not zero. Thus the reduced matrix elements of the K^{th} multipole of the OBDM are given by

$$\begin{aligned} \langle A\lambda J || (a_{n_1 l_1 j_1}^\dagger \tilde{a}_{n_2 l_2 j_2})^{(K)} || A\lambda J \rangle &= \\ &= \frac{\sqrt{2J+1}}{\langle JMK0 | JM \rangle} \sum_{m_j} (-1)^{j_2+m_j} \langle j_1 m_j j_2 - m_j | K 0 \rangle \\ &\times \langle A\lambda JM | a_{n_1 l_1 j_1 m_j}^\dagger a_{n_2 l_2 j_2 m_j} | A\lambda JM \rangle. \end{aligned} \quad (\text{A17})$$

where $\langle A\lambda JM | a_{n_1 l_1 j_1 m_j}^\dagger a_{n_2 l_2 j_2 m_j} | A\lambda JM \rangle$ are the OBDM's in HO space defined in Eq. (A1). Note that the factor $\sqrt{2J+1}/\langle JMK0 | JM \rangle$ in this expression cancels against the same factor in the expression for $\rho_{\text{sf}}(\vec{r})$, Eq. (A11).

We can now efficiently perform the deconvolution, by using the Fourier transform properties of the multipole expansion of the local density

$$\int d^3\vec{r} \exp(i\vec{q} \cdot \vec{r}) \rho_{\text{sf}}^{(K)}(r) i^K Y_K^{*0}(\hat{r}) = \tilde{\rho}_{\text{sf}}^{(K)}(q) Y_K^{*0}(\hat{q}), \quad (\text{A18})$$

where the multipole component of the density in momentum space is expressed as

$$\tilde{\rho}_{\text{sf}}^{(K)}(q) = 4\pi \int j_K(qr) \rho_{\text{sf}}^{(K)}(r) r^2 dr \quad (\text{A19})$$

with j_K the spherical Bessel Functions of the first kind.

Thus the deconvolution of each multipole gives

$$\rho_{\text{ti}}^{(K)}(r) = \frac{1}{2\pi^2} \int j_K(qr) \frac{\tilde{\rho}_{\text{sf}}^{(K)}(q)}{\tilde{\rho}_{\text{cm}}(q)} q^2 dq \quad (\text{A20})$$

where

$$\begin{aligned} \tilde{\rho}_{\text{cm}}(\vec{q}) &= \frac{\tilde{\rho}_{\text{cm}}^{(0)}(q)}{2\sqrt{\pi}} \\ &= \frac{8\sqrt{2}}{\sqrt{\pi}} \nu^{3/2} \int_0^\infty \frac{e^{-2\nu R^2} \sin(qR)}{qR} R^2 dR \\ &= e^{-q^2/8\nu} \end{aligned} \quad (\text{A21})$$

For spherically symmetric nuclei, this deconvolution simplifies even further because we only have one term in the multipole expansion, $K = 0$

$$\rho_{\text{ti}}^{(0)}(r) = \frac{1}{2\pi^2} \int_0^\infty \frac{\sin(qr)}{qr} \frac{\tilde{\rho}_{\text{sf}}^{(0)}(q)}{\tilde{\rho}_{\text{cm}}(q)} q^2 dq, \quad (\text{A22})$$

and the 3-dimensional ti density is simply

$$\rho_{\text{ti}}(\vec{r}) = \frac{\rho_{\text{ti}}^{(0)}(r)}{2\sqrt{\pi}} \quad (\text{A23})$$

without any angular dependence.

Another advantage of the multipole expansion is that it allows for a straightforward calculation of the (sf or ti) density for any magnetic projection M , once the multipoles $\rho^{(K)}(r)$ are known. The multipoles $\rho^{(K)}(r)$ are completely determined from reduced matrix elements, which do not depend M . The only dependence of $\rho_{\text{sf}}(\vec{r})$ on M is entirely through the explicitly M -dependent Clebsch–Gordan coefficients in Eq. (A11).

Finally, the expressions here are specific for the local static density (the same final and initial state), but the extension to local transition densities is straightforward.

-
- [1] A. M. Shirokov, J. P. Vary, A. I. Mazur and T. A. Weber, Phys. Lett. B **644**, 33 (2007)
- [2] A. M. Shirokov, J. P. Vary, A. I. Mazur, S. A. Zaytsev and T. A. Weber, Phys. Lett. B **621**, 96 (2005)
- [3] A. M. Shirokov, A. I. Mazur, S. A. Zaytsev, J. P. Vary and T. A. Weber, Phys. Rev. C **70**, 044005 (2004)
- [4] P. Maris, A. M. Shirokov and J. P. Vary, Phys. Rev. C **81**, 021301 (2010)
- [5] P. Maris, J. P. Vary and A. M. Shirokov, Phys. Rev. C **79**, 014308 (2009)
- [6] S. K. Bogner, R. J. Furnstahl, P. Maris, R. J. Perry, A. Schwenk, J. P. Vary, Nucl. Phys. A **801**, 21-42 (2008)
- [7] B. D. Keister, W. N. Polyzou, J. Comput. Phys. **134**, 231-235 (1997)
- [8] M. A. Caprio, P. Maris and J. P. Vary, Phys. Rev. C. (to appear); arXiv:1208.4156

- [9] P. Navrátil, J. P. Vary and B. R. Barrett, Phys. Rev. C **62**, 054311 (2000).
- [10] K. Suzuki and S. Y. Lee, Prog. Theor. Phys. **64**, 2091 (1980); K. Suzuki, *ibid.* **68**, 246 (1982); **68**, 1999 (1982); K. Suzuki and R. Okamoto, Prog. Theor. Phys. **92**, 1045 (1994).
- [11] L. E. Marcucci, M. Pervin, S. C. Pieper, R. Schiavilla, R. B. Wiringa, Phys. Rev. C **78**, 065501, (2008).
- [12] D.H. Gloekner and D.R. Lawson, Phys. Lett. B **53**, 313 (1974).
- [13] P. Sternberg, E. G. Ng, C. Yang, P. Maris, J. P. Vary, M. Sosonkina, and H. V. Le, in the Proceedings of the 2008 ACM/IEEE conference on Supercomputing IEEE Press, Piscataway, NJ, 15:1-15:12 (2008).
- [14] P. Maris, M. Sosonkina, J. P. Vary, E. G. Ng, and C. Yang, Procedia CS **1**, 97-106 (2010).
- [15] P. Morse and H. Feshbach, *Methods of Theoretical Physics*, McGraw-Hill, New York (1953).
- [16] B. G. Giraud, Phys. Rev. C **77**, 014311 (2008).
- [17] P. Navrátil, Phys. Rev. C **70**, 014317 (2004).
- [18] I. Talmi, *Simple Models of Complex Nuclei*, Harwood Academic Publishers, Switzerland (1993).
- [19] A. Bohr and B. Mottelson, *Nuclear Structure*, W.A. Benjamin, New York (1969).
- [20] J. L. Friar, J. Martorell, and D. W. L. Sprung, Phys. Rev. A **56**, 4579 (1997).
- [21] W. Nortershauser, T. Neff, R. Sanchez, I. Sick, Phys. Rev. C **84**, 024307 (2011).
- [22] R. Sanchez *et al.*, Phys. Rev. Lett. **96**, 033002 (2006).
- [23] A. M. Shirokov, A. I. Mazur, J. P. Vary and E. A. Mazur, Phys. Rev. C **79**, 014610 (2009)
- [24] I. Stetcu, B. R. Barrett, P. Navrátil and J. P. Vary, Phys. Rev. C **73**, 037307 (2006)
- [25] R. Roth, T. Neff, H. Feldmeier, Prog. Part. Nucl. Phys. **65**, 50-93 (2010)
- [26] S. Vaintraub, N. Barnea, and D. Gazit, Phys. Rev. C **79**, 065501 (2009)
- [27] F. Ajzenberg-Selove, Nucl. Phys. A **490**, 1 (1988).
- [28] D.R. Tilley, C.M. Cheves, J.L. Godwin, G.M. Hale, H.M. Hofmann, J.H. Kelley, C.G. Sheu, and H.R. Weller, Nucl. Phys. A **708**, 3 (2002).
- [29] M. Pervin, S. C. Pieper, and R. B. Wiringa, Phys. Rev. C **76**, 064319, (2007).
- [30] S. C. Pieper, R. B. Wiringa, J. Carlson, Phys. Rev. C **70**, 054325 (2004)
- [31] S. C. Pieper, V. R. Pandharipande, R. B. Wiringa and J. Carlson, Phys. Rev. C **64**, 014001 (2001).
- [32] C. Forssen, E. Caurier, P. Navrátil, Phys. Rev. C **79**, 021303 (2009).
- [33] P. Navrátil, J. P. Vary, W. E. Ormand and B. R. Barrett, Phys. Rev. Lett. **87**, 172502 (2001)
- [34] U. van Kolck, Phys. Rev. C **49**, 2932 (1994).
- [35] E. Epelbaum, A. Nogga, W. Gloeckle, H. Kamada, U. G. Meissner and H. Witala, Phys. Rev. C **66**, 064001 (2002)
- [36] D. R. Entem and R. Machleidt, Phys. Rev. C **68**, 041001 (2003)
- [37] A. Nogga, P. Navrátil, B. R. Barrett and J. P. Vary, Phys. Rev. C **73**, 064002 (2006)
- [38] D.R. Tilley, J.H. Kelley, J.L. Godwin, D.J. Millener, J.E. Purcell, C.G. Sheu, and H.R. Weller, Nucl. Phys. A **745**, 155 (2004).
- [39] G. Audi, O. Bersillon, J. Blachot, A.H. Wapstra Nucl. Phys. A **729**, 3 (2003).
- [40] R. Roth, P. Navrátil, Phys. Rev. Lett. **99**, 092501 (2007).
- [41] R. Roth, Phys. Rev. C **79**, 064324 (2009)
- [42] T. Dytrych, K. D. Sviratcheva, C. Bahri, J. P. Draayer, J. P. Vary, J. Phys. G **35**, 095101 (2008).
- [43] T. Abe, P. Maris, T. Otsuka, N. Shimizu, Y. Utsuno and J. P. Vary, in New Faces of Atomic Nuclei, AIP Conf Proc 1355, **173** (2011); arXiv:1107.1784
- [44] T. Abe, P. Maris, T. Otsuka, N. Shimizu, Y. Utsuno and J. P. Vary, arXiv:1204.1755
- [45] Wolfram Research, Inc., *Mathematica*, Version 8.0, Champaign, IL (2010).
- [46] G. R. Satchler, *Direct Nuclear Reactions*, Clarendon Press, Oxford (1983).